

Hidden Connectivity Structures Control Collective Network Dynamics

Lorenzo Tiberi^{1,2,3}, David Dahmen¹, and Moritz Helias^{1,2,3}

¹*Institute of Neuroscience and Medicine (INM-6) and Institute for Advanced Simulation (IAS-6) and JARA-Institute Brain Structure-Function Relationships (INM-10), Jülich Research Centre, Jülich, Germany*

²*Institute for Theoretical Solid State Physics, RWTH Aachen University, 52074 Aachen, Germany and*

³*Center for Advanced Simulation and Analytics, Forschungszentrum Jülich, 52425 Jülich, Germany*

A common approach to model local neural circuits is to assume random connectivity. But how is our choice of randomness informed by known network properties? And how does it affect the network's behavior? Previous approaches have focused on prescribing increasingly sophisticated statistics of synaptic strengths and motifs. However, at the same time experimental data on parallel dynamics of neurons is readily accessible. We therefore propose a complementary approach, specifying connectivity in the space that directly controls the dynamics – the space of eigenmodes. We develop a theory for a novel ensemble of large random matrices, whose eigenvalue distribution can be chosen arbitrarily. We show analytically how varying such distribution induces a diverse range of collective network behaviors, including power laws that characterize the dimensionality, principal components spectrum, autocorrelation, and autoreponse of neuronal activity. The power-law exponents are controlled by the density of nearly critical eigenvalues, and provide a minimal and robust measure to directly link observable dynamics and connectivity. The density of nearly critical modes also characterizes a transition from high to low dimensional dynamics, while their maximum oscillation frequency determines a transition from an exponential to power-law decay in time of the correlation and response functions. We prove that the wide range of dynamical behaviors resulting from the proposed connectivity ensemble is caused by structures that are invisible to a motif analysis. Their presence is captured by motifs appearing with vanishingly small probability in the number of neurons. Only reciprocal motifs occur with finite probability. In other words, a motif analysis can be blind to synaptic structures controlling the dynamics, which instead become apparent in the space of eigenmode statistics.

Random matrices have been employed to describe the most disparate physical systems [1, 2], starting from nuclear energy levels in the 1950s [3]. Also in models of local cortical circuits, synaptic variability is often described as a random connectivity matrix [4–7]. Differently than typical physical systems, however, neural networks can learn their interaction structure: Through plasticity, synapses can organize into *ad hoc* configurations to perform specific computational tasks. It is therefore important to carefully ask how a neural network's function informs and constrains synaptic statistics. How do different choices of random connectivity affect the network dynamics, and eventually its function? And how is such choice informed by experimental evidence?

A common approach is to specify certain synaptic statistics [8, 9] based on experimental data on synaptic strengths and motifs [10]. Still, there is also another large part of experiments which focuses on the parallel dynamics of neurons, rather than their microcircuitry. Neuronal activity is typically analyzed with regard to dynamical properties such as its relaxation [11–13], correlations [14], dimensionality [15–17], and principal components spectrum [17]. Often, these quantities also characterize the network's computational mechanisms and performance [16, 17]. Therefore, these measures could potentially be used to infer properties of a network's connectivity based on its dynamics and function. For example, the aforementioned quantities are ubiquitously found to follow power laws: their exponents could be minimal and robust parameters linking observed dynamics and connectivity. In general, a theoretical framework is needed

that directly links measures of network dynamics to connectivity parameters. To this end, we propose a novel approach, which models connectivity in the space that directly controls the dynamics – the space of eigenmodes.

In Section I we introduce our *dynamics space approach* to modeling connectivity. This proceeds symmetrically with respect to the more traditional *synaptic space approach* (Fig. 1). In the latter, one imposes structure on the connectivity by fixing its synaptic strength statistics, such as the relative abundance of connectivity motifs. The corresponding statistics of the connectivity's eigenmodes is then derived analytically. In our approach, instead, we impose structure by fixing properties of the connectivity's eigenmodes, i.e. its eigenvalues and eigenvectors. We then develop a random matrix theory to derive the corresponding synaptic strengths statistics.

This in particular allows prescribing any shape for the connectivity's eigenvalue distribution. In Section II we show how the shape of the eigenvalue distribution directly impacts the network dynamics. It controls the power-law exponents characterizing the time-decay of correlation and response functions (II A) and the slope of the neuronal activity's principal components spectrum (II C). We expose how this is a generalization of the mechanism by which the distribution of Fourier modes controls the scaling properties of classical critical phenomena. Furthermore, the shape of the eigenvalue distribution controls two transition phenomena: a transition from power-law to exponential time-decay of the correlation and response functions (II A), and a transition from high to low

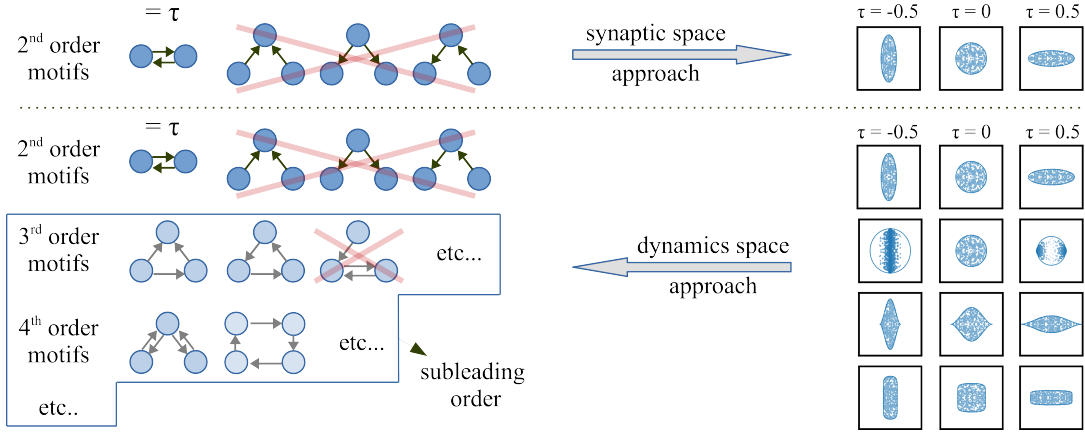


Figure 1. Schematic representation of the synaptic vs dynamics space approach. Top: synaptic space approach. Some motif statistics are assumed (left) and the eigenmode statistics (right) are derived. Specifically, here we show an archetypal approach which assumes only the presence of second order reciprocal motifs (here parameterized by τ , Eq. (2)). The corresponding eigenvalue distribution is uniform on an ellipse. The eigenvalues are relatively more spread along the real/imaginary axis depending on the value of τ . Bottom: dynamics space approach. We specify the eigenmode statistics, in particular allowing for any desired shape of the eigenvalue distribution (right). The derived synaptic statistics (left) predict only reciprocal motifs to leading order, as in the archetypal approach. These are parameterized again by the relative spread τ of the eigenvalues, here generalized to any distribution shape. Higher order motif structures are present, but are subleading in the number of neurons. Thus, the synaptic structures responsible for different shapes of the eigenvalue distribution (thus different dynamics) are hidden to a motifs analysis.

dimensional activity of neurons (IIB).

Which synaptic structures correspond to such wide range of dynamical behaviors? In Section III we derive the synaptic strength statistics for our connectivity ensemble. In IIIB we expose the most important result of the section, schematized in Fig. 1: the synaptic structures controlling the aforementioned dynamics are hidden to a motifs analysis, being reflected only by motifs occurring with vanishingly small probability. These structures instead become apparent to a spectral analysis of the connectivity, through the different shapes of the eigenvalue distribution.

Finally, in Section IV we discuss the relevance and outlooks of our work. In particular we discuss how, in modeling neuronal networks, one can impose further structure on their connectivity by fixing properties of its eigenvalue distribution, and how these properties could be inferred from observed network dynamics.

I. SETTING

We consider the recurrent network of linear rate neurons

$$\tau \partial_t x_i(t) = -x_i(t) + \sum_j J_{ij} x_j(t) + \xi_i(t), \quad (1)$$

where $x_i(t)$ is the rate activity of neuron i at time t ; $i = 1, \dots, N$. J_{ij} describes the recurrent connection from neuron j to i . τ is the characteristic timescale

of neuronal response. The network is driven by Gaussian white noise $\xi_i(t)$, with zero mean and variance $\langle \xi_i(t) \xi_j(t') \rangle = D \delta_{ij} \delta(t - t')$. In the following, we consider Eq. (1) in dimensionless units, setting $\tau = D = 1$. In the linear regime, the second order statistics of various network models, comprising integrate-fire and inhomogeneous Poisson neurons, is well captured by Eq. (1) [18–22]. For this reason, Eq. (1) is a minimal model for characterizing network dynamics analytically, as a function of J [9, 21, 23, 24].

Local neural circuits present strong variability in their connectivity. A common minimal approach is to model such variability as disorder, choosing J as a random matrix. Most likely, brain networks are not completely disordered: we expect them to have some function, thus some underlying connectivity structure. In the random connectivity setting, information about the network function or structure can be included in the model through the choice of statistics for J .

In previous works, the choice for the statistics of J has been inspired by the available experimental information regarding the connectivity structure of brain networks. For example, various works [8, 9, 24] have considered connectivity motifs [10], that is the occurrence of certain subgraphs with higher chance than random. These can be modeled by a non-vanishing moment of the elements of J involved in the motif [9]. In an archetypal approach [4, 25], for example, J is assumed Gaussian with statistics

$$g^2 \equiv N \langle J_{ij}^2 \rangle \quad \tau \equiv \langle J_{ij} J_{ji} \rangle / \langle J_{ij}^2 \rangle, \quad i \neq j. \quad (2)$$

Only two parameters are present: the synaptic gain g models the overall strength of recurrent connections,

while the degree of (anti)symmetry τ controls correlations between reciprocal connections, which can be associated with an abundance of reciprocal motifs. Note that any other second order motif (convergent, divergent, or chain) can be introduced as a low rank perturbation to this connectivity [9]. Throughout the manuscript, we will refer to this connectivity choice as the archetypal choice for J and use it for comparison with our approach.

Rather than starting from direct measures of the network structure (e.g. motifs), in this work we want to start from measures of the network function, i.e. its dynamical behavior, to inform the modeling choice of J . Indeed, there is also a wealth of experimental data recording the parallel dynamics of neurons, other than their microcircuitry. This data could be used to infer further structures in a connectivity, which, as we later show, are hardly noticeable by a direct measure of its motifs statistics. Furthermore, we note that analytical works deriving the network dynamics from the connectivity are typically restricted to motifs only up to second order [8, 9, 24]. While even these simple connectivity patterns have been shown to considerably impact the network dynamics, they are unlikely to fully capture the complex connectivity structure of brain networks. It is therefore important to complement the modeling of connectivity structures using the wealth of available information on the neuronal dynamics.

The main idea of this work is to specify the statistics of J in the space that directly controls the network dynamics: the space of eigenmodes. We can always decompose J into its eigenvalues λ_α and right eigenvectors V_α as

$$J_{ij} = \sum_{\alpha=1}^N V_{i\alpha} \lambda_\alpha V_{\alpha j}^{-1}, \quad (3)$$

where the left eigenvectors' matrix V^{-1} is the inverse of the right eigenvectors' matrix V . For typical random connectivity matrices, this decomposition can be performed without loss of generality (see Appendix A 1). Eigenvalues and eigenvectors have a direct dynamical interpretation: a linear combination of neurons $\sum_i V_{\alpha i}^{-1} x_i$ represents a collective mode of the linearized neuronal activity, with dynamical response $\propto \exp(-(1 - \lambda_\alpha)t)$. Thus, calling an eigenvalue $\lambda = \lambda_x + i\lambda_y$, the associated mode has decay constant $1 - \lambda_x$ and oscillation frequency λ_y . The distribution of eigenvalues associated with the connectivity J is therefore useful to characterize the dynamical repertoire available to the network. In fact, its knowledge has already proven important in the archetypal approach. In that case, eigenvalues are uniformly distributed on a centered ellipse in the complex plane [25] (Fig. 1, top). The transition to chaos occurring in the nonlinear regime, for example, is well understood, for $\xi = 0$, in terms of this ellipse crossing the line of linear instability, $\lambda_x > 1$ [4, 26, 27].

Rather than the standard *synaptic space approach*, in which the eigenmode statistics are derived from some specified synaptic strengths statistics, here we take a

symmetric, *dynamic space approach*, in which we define J through its eigenmode statistics, and later derive the corresponding synaptic strength statistics (Fig. 1). We define the eigenmode statistics as

$$\lambda \sim p(\lambda) \quad (4)$$

$$V = O + \nu G \quad (5)$$

Eq. (4) states that λ can be drawn from a distribution p of any arbitrary shape, provided its moments are bounded. One is therefore not constrained to a uniform elliptical distribution as in the archetypal approach, but can choose precisely what repertoire of decay constants and oscillation frequencies should be available to the network (see e.g. Fig. 1). In turn, we will show in Section II how the shape of p directly controls the dynamics, and thus can be fixed according to a certain observed or desired dynamical behavior of the network. The eigenvalues are drawn independently, following the same simplicity principle typically applied in the synaptic space approach: introducing minimal information in an otherwise disordered connectivity.

Following the same principle, we want to be agnostic regarding which direction a certain eigenmode takes in neuronal space. The eigenvector matrix V is therefore drawn independently from the eigenvalues. Eq. (5) defines it as a combination of a unitary and a complex Gaussian random matrix O and G , respectively, with interpolation parameter $\nu \in [0, 1]$ controlling the degree of non-normality of the network. A precise definition of O and G can be found in A 1. Intuitively, varying ν from 0 to 1 controls whether eigenmodes are orthogonal to each other ($\nu = 0$), or can take on more and more random, overlapping directions ($\nu \rightarrow 1$). The value $\nu = 1$ is an upper limit at which eigenvectors are too overlapping and the synaptic gain g diverges (see Section III).

A difference with the archetypal case of Gaussian J is that, there, eigenvalues and eigenvectors are found to be tightly correlated, and eigenvectors are in a strongly non-orthogonal regime similar to choosing $\nu \sim 1$ in our ensemble. In Section III we show that, in this strongly non-normal regime, a fine-tuned correlation structure is necessary to contrast the strong eigenvectors' overlap and thus keep the synaptic gain g of $\mathcal{O}(1)$. We then devise a method to initialize connectivities with such fine-tuned correlation structure, while still allowing for any shape of the eigenvalue distribution. In this way, through numerical simulations, we are able to characterize also the strongly non-normal regime. Including this strongly non-normal ensemble, our study therefore encompasses the archetypal case of Gaussian J .

As we show in Section II, varying the shape of the eigenvalue distribution causes a wide range of different dynamical behaviors. Surprisingly, however, we find this is not reflected by the leading order statistics of synaptic strengths. Just as for the archetypal connectivity, we find the synaptic strength statistics to be Gaussian, with only reciprocal motifs. In terms of the eigenmode statistics,

the leading order synaptic strength statistics are given by

$$g^2 = \frac{1 + \nu^2}{1 - \nu^2} \left(\langle \lambda_x^2 \rangle_\lambda + \langle \lambda_y^2 \rangle_\lambda \right) \quad (6)$$

$$\tau = \frac{1 - \nu^2}{1 + \nu^2} \frac{\langle \lambda_x^2 \rangle_\lambda - \langle \lambda_y^2 \rangle_\lambda}{\langle \lambda_x^2 \rangle_\lambda + \langle \lambda_y^2 \rangle_\lambda} \quad (7)$$

where $\langle \rangle_x$ denotes statistical averaging over the random variable x . Other second order motifs are absent. Higher order motifs are present, but only with a probability that is vanishingly small in the number of neurons, and would thus be very hard if not impossible to detect experimentally. As a result, connectivities with the same leading order motif structure can correspond to different eigenmode distributions, thus to very different network dynamics, as exemplified in Fig. 2. In other words, there are structures within a connectivity that have a strong impact in shaping the network dynamics, while remaining invisible to a motif analysis: these structures cannot be reduced to the generic abundance of certain connectivity patterns. However, these structures become apparent in terms of the spectral properties of the connectivity, specifically its eigenvalue distribution. Our findings on the synaptic strength statistics are discussed in more detail in Section III.

II. EFFECT ON DYNAMICS

In this section, we characterize how the eigenvalue distribution affects the network dynamics. It is natural to consider the shifted eigenvalues $k \equiv \lambda - 1$, that is the eigenvalues of the Jacobian $J - \mathbb{I}$ of the dynamics. Thus, calling $k \equiv k_x + \nu k_y$, a mode has decay constant k_x and oscillation frequency k_y .

We will focus on systems at the edge of criticality, that is with eigenvalue distributions touching the line of linear instability $k_x = 0$ from the right. Occasionally, we parameterize a small distance away from criticality by adding a small leak term $-\delta \cdot x$ to the *rhs* of Eq. (1). This effectively shifts the eigenvalues of the Jacobian $k \rightarrow k + \delta$, so the longest living modes have decay constant δ , rather than 0. Moving away from criticality through δ is equivalent to the more traditional rescaling of the spectral radius, through $J \rightarrow (1 + \delta)^{-1} J$, provided we also trivially rescale $t \rightarrow (1 + \delta)t$ and $D \rightarrow (1 + \delta)^{-1} D$ in Eq. (1). Here we use the former method, because δ appears naturally as a mass term, in an analogy with classical critical phenomena exposed later.

Studying the nearly critical regime is of particular interest because of the wealth of characteristic features of criticality, like power-laws, that are experimentally observed in brain networks [13, 14, 17], feeding the so-called critical brain hypothesis [28]. Theoretical works also suggest the edge of criticality as an optimal computational regime [29, 30].

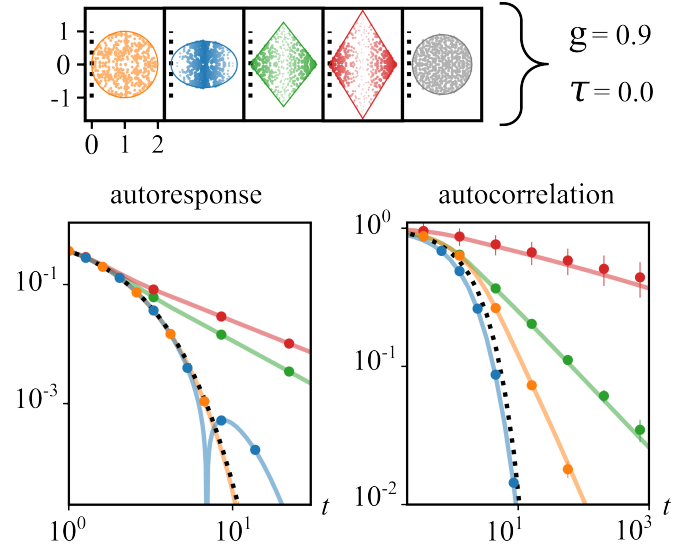


Figure 2. Same synaptic statistics correspond to different dynamics. Top: Various eigenvalue distributions, corresponding to different connectivities, which to leading order in the number of neurons share the same synaptic statistics. Specifically, $g = 0.9$ and $\tau = 0$ (Eq. (2)), corresponding to independently distributed synaptic strengths following Gaussian statistics. The eigenvalue distributions are plotted in the complex plane $k = 1 - \lambda$ and are nearly critical, touching the line of linear instability $k_x = 0$. The archetypal case of an exactly Gaussian connectivity with the same synaptic statistics is also shown in black. Bottom: Autocorrelation and autoresponse functions decay in time, colored accordingly. Despite sharing the same leading order synaptic statistics, the different connectivities feature different eigenvalue distributions, and thus correspond to very different network dynamics: the autocorrelation and autoresponse can either decay exponentially (blue, orange) or with power-laws with varying exponents (red, green). Curves: theory; markers: simulation; dotted, black line: known theory for the archetypal case of a Gaussian connectivity. Other parameters: For a given eigenvalue distribution, ν is fixed according to Eq. (6) and Eq. (7) so to have $g = 0.9$ and $\tau = 0$. Going from left to right in the top panel, $\nu = 0.49, 0.7, 0.52, 0.37$.

The main result of this section is that the density of nearly critical modes directly controls the power-law scaling exponents of various dynamical quantities: the population averaged autoresponse and autocorrelation function, the dimensionality of neural activity and the spectrum of its principal components. Precisely, we show that these are controlled by either of the exponents d or \bar{d} , controlling the density of nearly critical modes through $p(k_x) \xrightarrow{k \rightarrow 0} k_x^{d-1}$ or $p(\rho) \xrightarrow{k \rightarrow 0} \rho^{\bar{d}-1}$, where in the first case we consider approaching the critical point $k = 0$ along the real axis k_x , while in the second case along the radial direction ρ , having called $k \equiv \rho e^{i\phi}$. We call the exponent d the network's effective spatial dimension, in analogy with classical critical phenomena, as exposed later.

Close to criticality, the effect of the eigenvalue distribution on the dynamics is particularly apparent and can

be quantified in terms of power-law exponents. However, we note that our theory is not restricted to nearly critical systems: also away from criticality, varying the eigenvalue distribution has similar qualitative effects.

A. Autocorrelation and autoresponse

A common dynamical quantity considered in the study of disordered networks is the population averaged autocorrelation [4], $A(t) = \frac{1}{N} \sum_i \langle x_i(t) x_i(0) \rangle_\xi$. We also consider the population averaged autoresponse $r(t) = \frac{1}{N} \sum_i \lim_{\epsilon \rightarrow 0} \frac{1}{\epsilon} \langle x_i^\epsilon(t) - x_i(t) \rangle_\xi$, where $x_i^\epsilon(t)$ is the neural activity if Eq. (1) is perturbed by a term $\epsilon \delta(t)$ along direction i . In this subsection we show that the aforementioned functions have a power-law decay in time, whose exponent is controlled by the density of nearly critical modes. We also show a transition from exponential to power-law decay, controlled by the maximum oscillation frequency of nearly critical modes.

Standard linear response theory gives

$$r(t > 0) = \frac{1}{N} \sum_\alpha \exp(-k_\alpha t) \xrightarrow{N \rightarrow \infty} \int \mathcal{D}k \exp(-kt), \quad (8)$$

where in the last step we have taken the limit of the sum of eigenvalues to an integral over their probability density, with integration measure $\mathcal{D}k \equiv p(k) dk$, valid for large N . In this limit, using our random matrix theory (see Appendix B and the Supplemental Material [31]), we find $A(t)$ has the expression

$$A(t) = \frac{1 + \nu^2}{1 - \nu^2} \int \frac{\mathcal{D}k}{2k_x} \exp(-k|t|) - \frac{2\nu^2}{1 - \nu^2} \int \frac{\mathcal{D}k_1 \mathcal{D}k_2}{k_1 + k_2} \exp(-k_1|t|). \quad (9)$$

The autoresponse $r(t)$ depends only on the eigenvalue distribution, and not on the eigenvectors. The autocorrelation $A(t)$ instead also depends on the eigenvectors' distribution, as reflected by the parameter ν . The first term in Eq. (9) is the only one present in the limit of a normal network $\nu \rightarrow 0$, while the second term reflects a non-vanishing overlap between eigenvectors in the non-normal case (see Appendix B). For reference, we also report the known expression for the archetypal choice of a Gaussian connectivity, in the $\tau = 0$ case: $r(t > 0) \stackrel{\delta \rightarrow 0}{\sim} \exp(-t)$ and $A(t) \stackrel{\delta \rightarrow 0}{\sim} \frac{D}{4\delta} \exp(-\delta t)$.

Before looking at the time dependence of $r(t)$ and $A(t)$, it is instructive to focus on the equal-time variance $A(0)$ to introduce the concept of the network's effective spatial dimension. As for the archetypal choice of J , the variance can diverge as we approach criticality $\delta \rightarrow 0$. It's divergent behavior near criticality is described by the exponent d characterizing the density of nearly critical modes

$$p(k_x) \stackrel{k_x \rightarrow 0}{\sim} k_x^{d-1}. \quad (10)$$

Indeed, we can note that, when the variance diverges, the first term in Eq. (9) dominates, behaving like

$$\sim \int \frac{p(k_x) dk_x}{k_x + \delta} \sim \int \frac{k_x^{d-1} dk_x}{k_x + \delta} \propto \begin{cases} \delta^{d-1} & d < 1 \\ \text{const} & d > 1 \end{cases}, \quad (11)$$

where we performed the integration over the dummy variable k_y and introduced the small distance δ from criticality.

An analogous expression to Eq. (11) can be found for the variance of classical critical phenomena [32–34]. In fact, one can note that for a very special choice of J , Eq. (1) becomes the stochastic heat equation, a linear model of reference for out of equilibrium critical phenomena [33, 34]. Specifically, one may choose J such that $J - \mathbb{I}$ implements a discretization of the Laplace operator (i.e. the kinetic term) on a d -dimensional lattice. Then, the connectivity eigenmodes are the Fourier modes, with associated wave-vector \vec{k} . The density of nearly critical modes obeys $p(\|\vec{k}\|) \sim \|\vec{k}\|^{d-1}$, where d cannot be chosen arbitrarily as in this work, but corresponds to the system's spatial dimension. In analogy, we call d the network's effective spatial dimension, which in this work can also take non-discrete values. As for the stochastic heat equation, we identify through Eq. (11) a dimension $d_0 = 1$ above which the variance remains finite, while for smaller d it diverges as we approach criticality $\delta \rightarrow 0$. We further discuss the potential implications of this analogy in Section IV.

Having introduced the network's effective spatial dimension, we shall now focus on the asymptotic long-time dependence of $r(t)$ and $A(t)$. As for $A(0)$, this is naturally characterized by the marginal distribution $p(k_x)$ of decay constants of nearly critical modes, through the exponent d . In addition, the conditional distribution of oscillation frequencies $p(k_y|k_x)$ for a given decay constant is now important. We find this quantity to control whether the decay in time is power-law or exponential. Differently than for $A(0)$, a characterization for a generic $p(k_y|k_x)$ is hard in this case. To enlighten the role of oscillation frequencies, we consider the case of a uniform distribution of oscillation frequencies

$$p(k_y|k_x) = \theta(B(k_x) - |k_y|), \quad B(k_x) \stackrel{k_x \rightarrow 0}{\sim} k_x^b. \quad (12)$$

As illustrated in Fig. 3, two exponents characterize the distribution of nearly critical modes. Exponent d characterizes the density of nearly critical modes Eq. (10), while exponent b characterizes the maximum oscillation frequency of nearly critical modes $|k_y|_{\max} \propto k_x^b$, i.e. the boundary of the eigenvalue distribution. We find these exponents also characterize the dynamics in a very direct way, as illustrated in Fig. 3. Exponent b controls how the autocorrelation and autoresponse decay in time (Fig. 3(b)). In particular, it determines a transition from a slow power-law decay to a faster decay: for slow enough oscillations of nearly critical modes ($b \geq 1$) we have the

power-law decay; when oscillations are too fast ($b < 1$), instead, the decay is slower, potentially exponential and oscillating. Exponent d controls the power-law exponent in the case of exponential decay (Fig. 3(a)): $r(t) \sim t^{-d}$ and $A(t) \sim t^{-(d-1)}$.

Considering $r(t)$ as an example, this can be easily seen by integrating Eq. (8) over k_y and passing to the dimensionless variable $p \equiv k_x t$, obtaining

$$r(t) \stackrel{t \rightarrow \infty}{\sim} \frac{1}{t^{d+2}} \int_0^\infty dp p^d \exp(-p) \sin(p^b t^{1-b}) \quad (13)$$

We can see that, if $b > 1$, oscillations are unimportant in the long-time limit, as we can expand the oscillating term $\sin(x) \sim x$ in the integrand, recovering the power-law scaling $r(t) \sim t^{-d}$. If $b < 1$, instead, oscillations interfere with the build up of nearly critical modes into a pure power law.

The reasoning is completely analogous for $A(t)$, noting that the first term in Eq. (9) dominates in the long-time limit. This means that, though the degree ν of non-normality of the network affects quantitatively $A(t)$, it does not affect its power-law decay exponent. This is illustrated in Fig. C1.

Note that in the archetypal case of a Gaussian connectivity, the decay of both $r(t)$ and $A(t)$ is known to be exponential. The emergence of power-laws is a novelty of certain connectivities here considered, whose nearly critical modes have sufficiently slow oscillation frequencies ($b > 1$). This is of relevance for the ubiquitous observation of power-laws in neural dynamics. For example, a power-law behavior in the response function could be relevant for the phenomenon of neural avalanches [11–13]. In particular, the recently observed variability in avalanches' power-law exponents [13] may be explained by the network fluctuating in its operational point. This would cause fluctuations in its effective connectivity, thus in particular in the parameter d controlling the power-law exponents.

Another difference with the archetypal Gaussian connectivity is in the fact that there are connectivities in our ensemble, all those with $d > d_0 = 1$, for which $A(0)$ remains finite even at criticality ($\delta \rightarrow 0$). Notice that this includes the case of a uniform elliptical eigenvalue distribution, as found in the archetypal connectivity, which has $d = 1.5 > d_0$. This apparent inconsistency is due to the fact that the archetypal connectivity is also constrained to having strongly non-orthogonal eigenvectors, similar to sending $\nu \rightarrow 1$ in our ensemble, and a fine-tuned correlation structure between eigenvalues and eigenvectors. We study this regime in III C and see that indeed the variance diverges in this case.

We conclude remarking that the power-law scaling found in this section, but also in the following sections, only depend on a very generic property of the eigenvalue distribution, namely the scaling Eq. (10). Other properties of the eigenvalue distribution can affect quantitatively the shape of $A(t)$ and $r(t)$, but are irrelevant with regards to the power-law scaling. For example, Fig. 3(b)

(cases $b = 1.0, 1.5$) illustrates how varying the shape of the distribution boundary, here controlled by b , does not affect the power-law exponents, which is fixed by d . We further exemplify this in Fig. C1. For example, we also show how the power-law scaling is not altered by a stretching of the eigenvalue distribution along the imaginary axis (cf. Eq. (A1)). By Eq. (7), this alters the degree of symmetry τ of the connectivity matrix. Thus, in particular, also symmetry does not affect the power-law decay exponent.

B. Dimensionality

In this subsection we characterize a transition from high to low dimensional activity, controlled by the density of nearly critical modes.

A common measure of neuronal activity is its covariance matrix. Here we consider the equal-time covariance $C_{ij} = \langle x_i(t) x_j(t) \rangle$ and the long time-window covariance $C_{ij} = \lim_{T \rightarrow \infty} \frac{1}{T} \langle \hat{x}_i(0) \hat{x}_j(0) \rangle$, where we defined the Fourier transformed neural activity $\hat{x}_i(\omega) = \int_{-\frac{T}{2}}^{\frac{T}{2}} dt e^{-i\omega t} x_i(t)$. A common analysis of the covariance is by its principal components. The covariance C being positive semi-definite, one can always consider its eigenmode decomposition

$$C = \sum_{\alpha} U_{\alpha} c_{\alpha} U_{\alpha}^T \quad (14)$$

with the eigenvectors U_i identifying orthogonal directions of neuronal variability, and the eigenvalues $c_i \geq 0$ its intensity along that direction. Recent research has shown considerable interest for the dimensionality of neuronal activity [17, 35, 36], which is an estimate of how many of the strongest principal components are required to explain most of neuronal variability. Various experimental studies have found low dimensional activity in the brain [15–17], and sufficiently low dimensionality is argued to be necessary for optimal stimulus encoding [17]. A common measure of dimensionality is the participation ratio [9, 24]

$$D \equiv \frac{(\sum_{\alpha} c_{\alpha})^2}{\sum_{\alpha} c_{\alpha}^2} = \frac{(\text{Tr}[C])^2}{\text{Tr}[C^2]}, \quad (15)$$

which can conveniently be reduced to traces of powers of the covariance matrix. The latter we are able to compute with our random matrix theory (see Appendix B and the Supplemental Material [31]). We now proceed to characterize the behavior of dimensionality near criticality.

1. Equal time covariance

Let us start considering the equal-time covariance. Once again, we find that dimensionality is controlled by the density of nearly critical modes Eq. (10) through the exponent d .

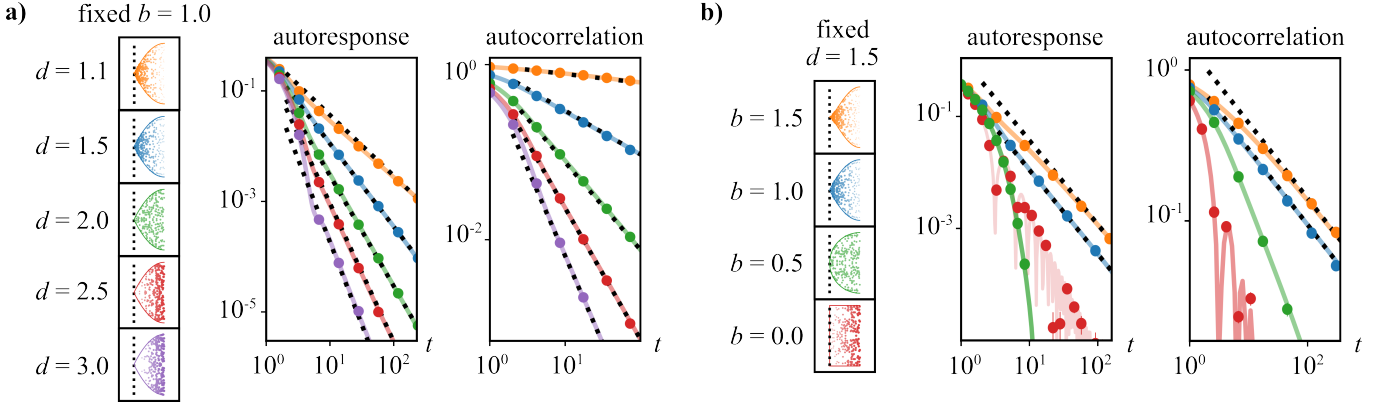


Figure 3. (a) Power-law decay controlled by d . On the left, different distributions of nearly critical eigenvalues are shown in the k_x - k_y plane for fixed $b = 1$ and varying d . The dashed vertical line represents the critical line of instability at $k = 0$. Corresponding decay in time of the autoresponse $r(t)$ and normalized autocorrelation $A(t)/A(0)$, colored accordingly. Solid curves: theory; markers: simulations; dashed, black lines: power-law decay with exponent d for the autoresponse and $d - 1$ for the autocorrelation. (b) Transition from power-law to faster decay, controlled by b . The autoresponse and normalized autocorrelation are shown for fixed $d = 1.5$ and varying b . Solid curves: theory; markers: simulation. For $b \geq 1$, we see a power law decay (dashed, black lines), with the same exponent fixed by the value of d , regardless of the value of b . For $b < 1$ the decay is faster. Other parameters: $N = 10^2$, $\nu = 1/\sqrt{3}$.

The full expression for the dimensionality is made intricate by its dependence on the degree ν of non-orthogonality, and is given in the Supplemental Material [31]. Just as for the autocorrelation, however, we can get a direct intuition of its shape by looking at the dominating term near criticality ($\delta \rightarrow 0$). Note the numerator in Eq. (15) corresponds to $A(t=0)^2$ given in Eq. (9). We already discussed its diverging behavior near criticality in Eq. (11). The full expression for the denominator $\text{Tr}[C^2]$ is lengthy and is reported in the Supplemental Material [31]. The expression is analogous to Eq. (9), containing a first term surviving for $\nu \rightarrow 0$, which is the one dominating the divergent behavior near criticality $\delta \rightarrow 0$, in addition to terms due to the network non-normality, analogous to the second term in Eq. (9). The dominating divergent term behaves as

$$\sim \int \frac{p(k_x) dk_x}{(k_x + \delta)^2} \sim \int \frac{k_x^{d-1} dk_x}{(k_x + \delta)^2} \propto \begin{cases} \delta^{d-2} & d < 2 \\ \text{const} & d > 2 \end{cases}. \quad (16)$$

Combining Eq. (11) and Eq. (16) into Eq. (15), we therefore distinguish the behavior of dimensionality into three regions: for $d > 2$, dimensionality is finite even at criticality; for $1 < d < 2$ we have low-dimensional activity, decaying as δ^{2-d} ; for $d < 1$ again we have low-dimensional activity, but decaying as δ^d . As can be seen in Fig. 4(a), we therefore have a transition from high to low dimensional activity at $d = 2$. The transition becomes infinitely sharp at criticality. Otherwise, dimensionality shows an optimum for connectivities with dimension $d \sim 1$, at which the dimensionality of the input noise is reduced the most. As we discuss in Section IV, this observation may also be interesting for initializing the connectivity of artificial networks at an optimal starting point for dimensionality reduction, from which to begin the network

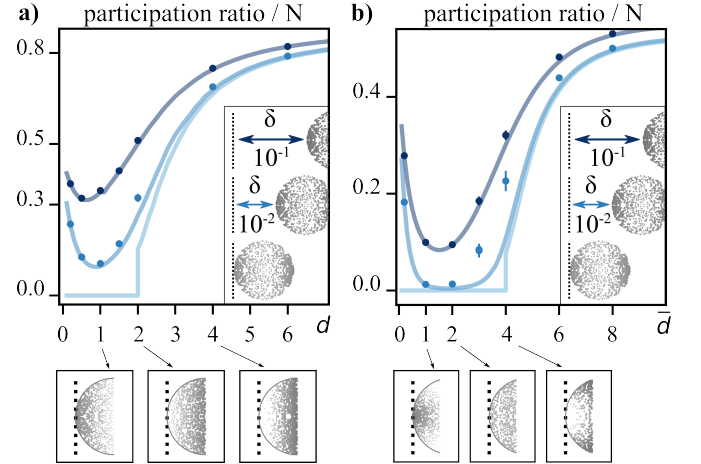


Figure 4. Transition from high to low dimensionality. (a) participation ratio for the equal-time covariance, as a function of d . Curves in lighter blue correspond to decreasing values of δ (see inset). Solid curves: theory; markers: simulation. Only theory is shown for $\delta = 0$ (lightest blue), at which the transition is infinitely sharp. At the bottom, distributions of nearly critical eigenvalues are shown for some example values of d . (b) is analogous to (a), showing the participation ratio for the long time-window covariance as a function of d . Note an eventual offset between theory and simulation for the smaller δ is due to finite size effects (see Fig. S1 in the Supplemental Material [31]). Other parameters: (a) $N = 10^3$, $\nu = 1/\sqrt{3}$, $b = 0.5$; (b) $N = 8 \cdot 10^3$.

training. Finally, note how the asymptotic description we have just given well describes the full analytical expression for the dimensionality even further away from criticality, e.g. for $\delta = 0.1$.

Once again, we show in Fig. C1 that both the degree of

non-normality and other details in the shape of the eigenvalue distribution do not affect qualitatively our predictions.

2. Long time-window covariance

For the long-time window covariance the reasoning is completely analogous. Integrals of the same kind as Eq. (11) appear (see Appendix B). The main difference is that in Eq. (11), the relevant direction of integration approaching the critical point $k = 0$ was the one along the real axis, k_x . Instead, for the long-time window covariance the relevant direction is the radial one, ρ , where we defined $k \equiv \rho e^{i\phi}$. We therefore introduce a radial dimension \bar{d} controlling the density of nearly critical modes along the radial direction

$$p(\rho) \stackrel{\rho \rightarrow 0}{\sim} \rho^{\bar{d}-1} \quad (17)$$

The results are then completely analogous to those for the equal-time covariance, and are shown in Fig. 4(b). For $\bar{d} > 4$, dimensionality is constant even at criticality; for $2 < \bar{d} < 4$ we observe low-dimensional activity, decaying as $\delta^{4-\bar{d}}$; for $\bar{d} < 2$ again we have low-dimensional activity, but decaying as $\delta^{\bar{d}}$. Close to criticality, dimensionality will show an optimum for connectivities with dimension $\bar{d} = 2$, at which the dimensionality of the input noise is reduced the most. Note that in the archetypal case of Gaussian J , the decay of dimensionality is known to behave like δ^2 [9, 23, 24]. This is reproduced also for our matrix with matching distribution of eigenvalues (i.e. uniform on the circle). Indeed, such distribution has radial dimension $\bar{d} = 2$. Interestingly $\bar{d} = 2$ is also where we have an optimal reduction of the dimensionality of input noise. Note, however, that many shapes of the eigenvalue distribution other than circular uniform can have $\bar{d} = 2$.

C. Principal components spectrum

The participation ratio Eq. (15) is a quantity derived from the first two moments of the principal components eigenvalues c , appearing in Eq. (14). It is also interesting to study the full distribution $p(c)$ of these eigenvalues. For example, a recent experimental study has considered the principal components of neural activity in V1 of mice, during the encoding of image stimuli [17]. They plot the eigenvalues c against their rank, that is their ordering from largest to smallest. They find a power-law decay with exponent $\alpha = 1$, which they theoretically argue to be optimal for encoding visual stimuli: larger α would correspond to fewer details encoded, while a smaller α would be too sensitive to details and correspond to a fractal representation. Recent theoretical work has derived a similar power-law decay for a network governed by Eq. (1), for the archetypal choice of J [9]. They find a power-law exponent of $\alpha = 1.5$, different from the one

experimentally observed. Here we show how the density of nearly critical modes controls this exponent, thus identifying a structural property in the connectivity that can tune it to the optimal value observed experimentally.

Deriving an expression for $p(c)$ for any value of the degree of non-normality ν is a hard task that we leave for future work. However, we can easily derive $p(c)$ for the normal case $\nu = 0$, and study numerically what happens for $\nu \neq 0$.

Let us first consider the principal components of the time integrated covariance. For $\nu = 0$, the principal components eigenvalues c are simply related to the connectivity eigenvalues $k = \rho e^{i\phi}$ by $c = \rho^{-2}$ (see Appendix B). Therefore, $p(c) = p(\rho(c)) c^{-\frac{3}{2}}$. Once again, we see that a power-law emerges, that is controlled by the density of nearly critical modes Eq. (17): $p(c) \stackrel{c \rightarrow \infty}{\sim} c^{-\frac{\bar{d}+2}{2}}$. It follows that the power-law decay of c with its rank n is $c \sim n^{-\alpha}$, with $\alpha = 2/\bar{d}$. Therefore, as illustrated in Fig. 5(a), varying the connectivity's density of nearly critical modes tunes the power-law decay of the principal components spectrum. Numerically, we find that also the degree of non-normality ν can partially control the decay exponent. As illustrated in Fig. 5(b), for a fixed \bar{d} , increasing ν increases the exponent α . This effect is weak for small or intermediate values of ν , and starts becoming apparent for large values of ν . Finally, let us note that a uniform elliptical eigenvalue distribution corresponds to $\bar{d} = 2$ and therefore to $\alpha = 1$ in our ensemble. This is different from the value $\alpha = 1.5$ found for the archetypal J , which has the same eigenvalue distribution. The difference is caused by the different statistics for the eigenvectors, which in the archetypal case are strongly non-orthogonal and correlated to the eigenvalues. Interestingly, the exponent $\alpha = 1.5$ is approached in our case by increasing ν to higher degrees of non-normality $\nu \sim 0.85$. We characterize the strongly non-normal regime in III C, finding a similar qualitative dependence of α on \bar{d} .

Previous work [9] has shown that α remains unaltered irregardless of the presence of any type of second order motifs. Our results show that there are other structures in a connectivity that can control this exponent, in particular tuning it to an optimal value for stimuli encoding [17]. Importantly, as mentioned in Section I and later discussed in Section III, these structures are invisible to a motif analysis, and only become apparent by inspecting the spectral properties of the connectivity.

As illustrated in Fig. 5(c-d), completely analogous results follow for the equal-time covariance. The only difference is that here $c = k_x^{-1}$ (see Appendix B), thus the power-law exponent α is still controlled by the density of nearly critical modes Eq. (10), but the one obtained approaching the critical point along the real axis. Specifically, we have a power-law decay with rank $c \sim n^{-\alpha}$, with $\alpha = 1/d$.

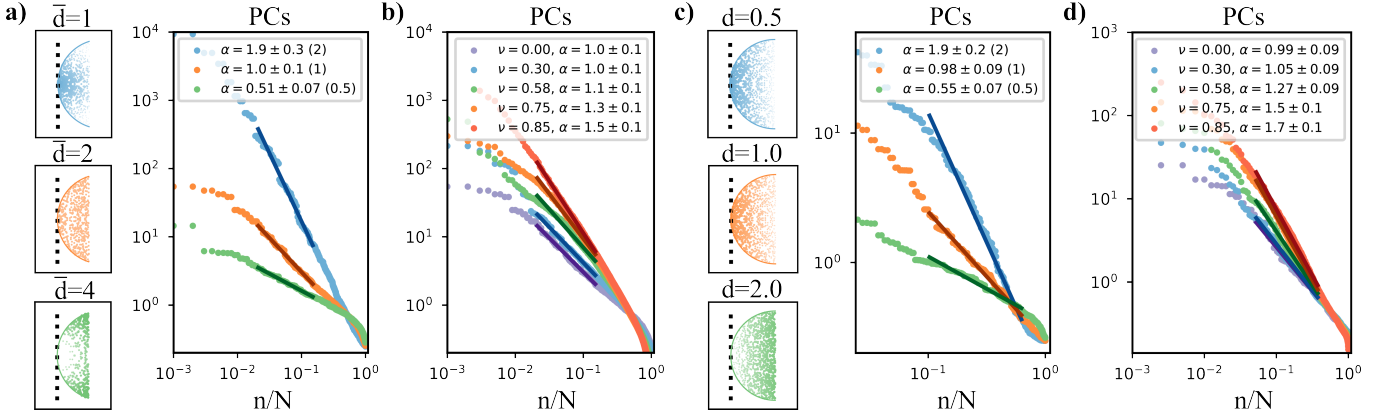


Figure 5. Connectivity controls the principal components spectrum. Covariance eigenvalues plotted against their fractional rank n/N . (a-b) Case of the long time-window covariance. (a) Case $\nu = 0$. Shown for connectivities having eigenvalue distributions with varying \bar{d} (shown on the left and colored accordingly). Markers: simulation; lines: fitting power-law; legend: mean and standard deviation of the power law exponent α , found for 48 independent realizations of the connectivity. Theoretical prediction in parenthesis. (b) Same as (a), but for fixed $\bar{d} = 2$ and varying ν (see legend). (c-d) Same as (a-b), but for the case of the equal-time covariance. In (c) we fix $\nu = 0$ and vary d . In (d) we fix $d = 1$ and vary ν . Other parameters: (a-b) $N = 10^3$, $\delta = 0.01$, $b = 0.5$; (c-d) $N = 4 \cdot 10^2$, $\delta = 0.01$.

III. CONNECTIVITY STATISTICS

In this section, we present in more detail our results deriving the synaptic strength statistics of the connectivity matrices in our ensemble.

A. Leading order synaptic statistics

First, we comment on the leading order synaptic statistics. To leading order, the connectivity is Gaussian and presents only reciprocal motifs, just as in the archetypal case. The synaptic strength statistics are given by Eq. (6) and Eq. (7). These expressions depend on both the degree of non-normality ν and the second moments of the eigenvalue distribution.

Let us first fix ν and discuss the effect of the eigenvalue distribution. Notice the synaptic gain g is controlled by the overall spread of eigenvalues on the complex plane. Unsurprisingly, increasing the spectral radius of the eigenvalue distribution corresponds to proportionally increasing the synaptic gain.

The degree of symmetry τ is instead controlled by the relative spread of the distribution along the real and imaginary axes. Notice that Eq. (7) generalizes to any eigenvalue distribution in our ensemble a fact that could already be observed for the elliptical distribution corresponding to the archetypal J : there, varying τ corresponds to stretching the ellipse along the imaginary or real axis (see e.g. Fig. 1). In fact, provided we choose $\nu^2 = \frac{1-\tau^2}{3+\tau^2}$, our ensemble reproduces the values of g and τ of the archetypal connectivity, when it is initialized with the same elliptical eigenvalue distribution. For the special case $\tau = 0$, we have to choose $\nu = 1/\sqrt{3} \sim 0.577$ (see Fig. 6(a)). Note, however, that the connectivities in the

two ensembles are still different: On the one hand, synaptic strength statistics of our ensemble have a more complicated subleading order structure, which accounts for the different possible shapes of the eigenvalue distribution. On the other hand, the archetypal connectivity has strongly non-orthogonal eigenvectors and a fine-tuned correlation structure between eigenvalues and eigenvectors, which we introduce in our analysis only later in III C.

For a fixed eigenvalue distribution, notice g and τ can still be partially tuned by the degree of non-normality ν . For example, stronger normality of the network (i.e. smaller ν) corresponds to stronger (anti)symmetry. Note that, as should be expected, perfect (anti)symmetry is only achieved in the special limit of a normal network $\nu = 0$ and an eigenvalue distribution collapsed on the (imaginary) real axis.

Regarding the effect of ν on the synaptic gain g , note that this remains of $\mathcal{O}(1)$ for considerably strong $\nu \sim 0.9$ (Fig. 6(a)). However, a too strong non-normality $\nu \rightarrow 1$ makes g diverge. More extreme degrees of non-normality require correlations between eigenvalues and eigenvectors, in order to keep g of order unity. We discuss this case in III C. Finally, note that this divergence of the synaptic gain is a non-trivial effect of the eigenvectors' non-orthogonality. It occurs for any fixed spectral radius of the eigenvalue distribution. In particular, it cannot be compensated by a trivial rescaling of the synaptic strengths, as this would also shrink the spectral radius.

B. Hidden synaptic structures

Despite the connectivity being Gaussian to leading order in N , it still contains all sorts of higher order statis-

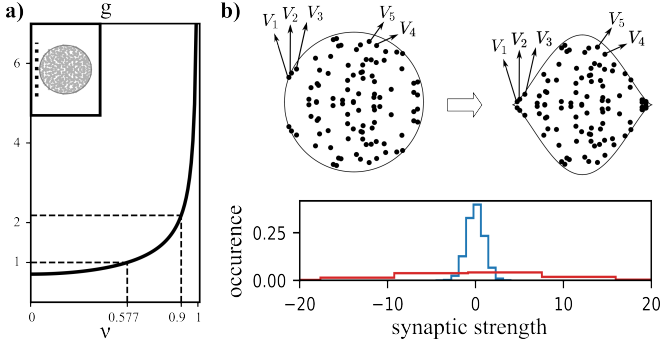


Figure 6. (a) Synaptic gain g as a function of the degree of non-normality ν , for the case of a uniform circular distribution (inset), as that found in the archetypal connectivity for $g = 1$ and $\tau = 0$. The dotted lines highlight the special value $\nu = 1/\sqrt{3} \sim 0.577$, for which $g = 1$ is recollected. Also the value $\nu = 0.9$ is highlighted, for which g is still of $\mathcal{O}(1)$. (b) Method for initializing connectivities with arbitrary eigenvalue distribution in the strongly non-normal regime. Top: starting from the archetypal Gaussian connectivity, we continuously shift its eigenvalues (left) into a new distribution (right). Each eigenvector remains associated to the original eigenvalue, so to preserve the tight correlation structure that ensures $g = \mathcal{O}(1)$. This can be checked in the blue histogram of scaled synaptic strengths $\sqrt{N}J_{ij}$ at the bottom, which has an $\mathcal{O}(1)$ variance. If instead the strongly non-normal eigenvectors were randomly assigned to the eigenvalues of the new distribution, we would have a divergent synaptic gain (red histogram).

tics. These are expected, as they must account for all eigenvalue distributions that are possible within our ensemble. The surprising result that we will show here, however, is that these higher order statistics appear only at subleading order in N .

Writing the connectivity in dimensionless units $\bar{J} := J\sqrt{\frac{N}{g}}$, we prove (see Appendix A 5 and the Supplemental Material [31]) that higher order cumulants $\langle\langle \bar{J}_{i_1 i_2} \dots \bar{J}_{i_{2n-1} i_{2n}} \rangle\rangle$ are of order $\mathcal{O}\left(\frac{1}{\sqrt{N}}\right)$ for $n = 3$ and of order $\mathcal{O}\left(\frac{1}{N}\right)$ for any other $n > 3$. We also prove that the only nonvanishing cumulants are those for which all indices i_1, \dots, i_{2n} are matched in pairs. For second order cumulants, this means only reciprocal motifs, associated with the cumulant $\langle\langle J_{ij} J_{ji} \rangle\rangle$, are present. For example, instead, cumulants like $\langle\langle J_{ij} J_{kj} \rangle\rangle$, $\langle\langle J_{ji} J_{jk} \rangle\rangle$ or $\langle\langle J_{ij} J_{jk} \rangle\rangle$, associated respectively with divergent, convergent, or chain motifs are null (see Fig. 1 for a schematic representation). For a numerical validation of our predictions on the synaptic strength statistics, see Fig. C2 and Fig. S6 in the Supplemental Material [31].

Note that, though correlations between synaptic strengths are present at all orders, their quick scaling with N is such that the central limit theorem still holds, so that statistical averages coincide with empirical averages for large N . For example, $\langle\langle J_{ij} J_{ji} \rangle\rangle \sim \frac{1}{N(N-1)} \sum_{i \neq j} J_{ij} J_{ji}$. The latter measure is closer to the

typical experimental procedure, where one does not compute statistics over different brains (i.e. different realizations of the connectivity), but rather averages empirically over all synaptic strengths within one brain (i.e. one realization of the connectivity).

The results here presented show that there can be structures within a connectivity, which, despite having a strong impact on the network dynamics, remain hidden to a motif analysis. Instead, these structures become apparent when inspecting the spectral properties of the connectivity, specifically its eigenvalue distribution. Indeed, we have shown in Section II how different shapes of the eigenvalue distribution control a wide range of dynamical behaviors. To a motif analysis, however, important differences in the eigenvalue distribution only manifest themselves through high order motifs appearing with vanishingly small probability at large N . This fact makes them potentially hard to detect, thus hidden. Note that this does not imply that connectivities which cause different dynamics only have weak structural differences. In fact, the structural differences are very apparent to a spectral analysis of the connectivity, specifically in the different shapes of the eigenvalue distributions. This suggests that these structural differences may be more collective in nature and thus hardly captured by a motif description that focuses on the average abundance of connectivity patterns involving only few neurons.

Our results show the importance of complementing a motif-based approach with a spectral approach, when characterizing or modeling connectivity in neuronal networks. This would ensure that connectivity structures that are important for the network dynamics are not overlooked. Notice that our approach, modeling connectivity from the eigenmode statistics, is complementary and does not exclude the typical approach imposing the motifs' statistics. Indeed, in the density of nearly critical eigenvalues we have identified a connectivity structure that can be fixed on top of the motifs' structures that are typically considered. For example, we have shown in III A that the abundance of reciprocal motifs is fixed by the relative spread of eigenvalues along the real and imaginary axis. This is another property of the eigenvalue distribution which can be tuned independently from the density of nearly critical eigenvalues. Furthermore, other second order motifs can always be included as low rank perturbations of the here considered connectivities [9].

C. Strongly non-normal regime

In this subsection we numerically extend our analysis to the case of strongly non-orthogonal eigenvectors. With this extension, our analysis encompasses the case of the archetypal choice of Gaussian connectivity. We will see that most results obtained in Section II qualitatively apply also to this regime.

In III A we noticed that the synaptic gain g diverges in the strongly non-normal regime $\nu \rightarrow 1$. In Appendix

A 2 we give an intuition for this divergence in terms of the eigenvalues of the eigenvector matrix. Here we rather focus on giving an intuition on how g can be kept of $\mathcal{O}(1)$ even in this strongly non-normal regime, and provide a method to explore this regime numerically.

It is instructive to inspect the archetypal Gaussian connectivity. This has $g = \mathcal{O}(1)$, while at the same time presenting strongly non-orthogonal eigenvectors (see Fig. S2 (a) in the Supplemental Material [31]). This is made possible by a fine-tuned correlation structure between eigenvalues and eigenvectors, which we do not have in our original ensemble. We can see this by randomly shuffling the association between eigenvectors and eigenvalues and then reconstruct the connectivity through Eq. (3): the synaptic gain then diverges with N , just like it does in our ensemble, in which no correlation structure is assumed (see Fig. S2 (b-c) in the Supplemental Material [31]). This shows that the original association was fine-tuned to tightly balance the summation on the r.h.s. of Eq. (3) to result in finite synaptic strengths.

Leveraging on these insights, we devise a method to initialize connectivities also in this strongly non-normal regime, while still allowing for any shape of the eigenvalue distribution. The idea is to preserve the necessary correlation structure found in the archetypal connectivity, even when choosing an eigenvalue distribution different than uniform elliptical. The method's details are given in Appendix A 4. The idea can be summarized as follows (Fig. 6(b)): We start from the archetypal J for $\tau = 0$, which naturally implements strongly non-normal eigenvectors and the necessary correlations with eigenvalues. It's eigenvalue distribution will be uniform on the circle. We obtain other eigenvalue distributions by continuously shifting the eigenvalues into some new position in the complex plane, such that they are distributed according to the new desired distribution. The intuition is that the continuous shift preserves to some extent the tight correlations between eigenvalues and eigenvectors, such that the connectivity remains well defined even if the eigenvectors are strongly non-orthogonal. We verify numerically that indeed this method ensures a well defined $g = \mathcal{O}(1)$ (see Fig. 6(b) and Fig. S2 in the Supplemental Material [31]). We call the ensemble of connectivities obtained with this method the *strongly non-normal ensemble*, and refer to the ensemble discussed in the rest of the manuscript, for which we derived analytical predictions, as *our original ensemble*.

Our numerical simulations for the strongly non-normal ensemble show that our theory developed for the original ensemble still qualitatively captures most of the phenomena described in Section II. As shown in Fig. 7(a-b), dimensionality as a function of the density of nearly critical modes, as parameterized by d or \bar{d} , presents a similar shape as that shown in Fig. 4. In particular, an optimum is present at which the dimensionality of the input noise is most reduced. As could be expected, it is for strong degrees of non-normality that our theory for the original ensemble is most similar to the here presented

simulations. Fig. S3 in the Supplemental Material [31] shows additional simulations further away from criticality. As can be seen in Fig. 7(c-d), d or \bar{d} also control the power-law decay exponent of the principal components spectrum. As we already noted in II C, the decay is steeper than in our original ensemble at $\nu = 0$, but is in fact very similar to our original ensemble at large ν . For the autoresponse function, the results are exactly the same as those found in the previous section, as this function does not depend on the eigenvector statistics. The only different behavior is shown by the autocorrelation function (see Fig. S4 in the Supplemental Material [31]). There, we find the autocorrelation to diverge in both its amplitude $A(0)$ and exponential decay time as $\delta \rightarrow 0$, even for $d > d_c$. Moreover, regardless of the value of b , the decay is always exponential, rather than power-law. This suggests that, in the case of the autocorrelation, the interplay between strong non-orthogonality and correlations between eigenvalues and eigenvectors has a role that is not qualitatively captured by our original ensemble.

Not only the dynamics, but also the motifs statistics of these strongly non-normal connectivities appear to be qualitatively captured by the theory for our original ensemble (see Fig. C2 and Fig. S6 in the Supplemental Material [31]). In particular our simulations suggest that, also in this case, hidden synaptic structures control the shape of the different eigenvalue distributions and hence the different dynamics.

IV. DISCUSSION

A. Summary of main findings

We have developed a novel approach that allows modeling a network's connectivity in the space of its eigenmodes. Previous works have identified the importance of connectivity eigenmodes as carrying relevant structures for the network dynamics and function [19, 37, 38]. The idea of shaping these structures has been explored, for example, through training the synaptic strengths [37] or modeling low-rank additions to a random bulk connectivity [39]. To the best of our knowledge, however, no previous work has provided an analytical method for modeling the random bulk connectivity directly in the eigenmodes space.

Our method imposes structure on a connectivity by specifying its eigenvalue distribution and the degree of non-orthogonality of its eigenvectors. We have shown in III B how these structures are hidden to a motif analysis: they are only reflected by hardly detectable motifs which appear with vanishingly small probability at large number of neurons. These structures can instead be clearly identified through a spectral analysis of the connectivity, in particular by inspecting the shape of its eigenvalue distribution.

These apparently hidden structures have a strong impact on the network dynamics. In Section II, we have

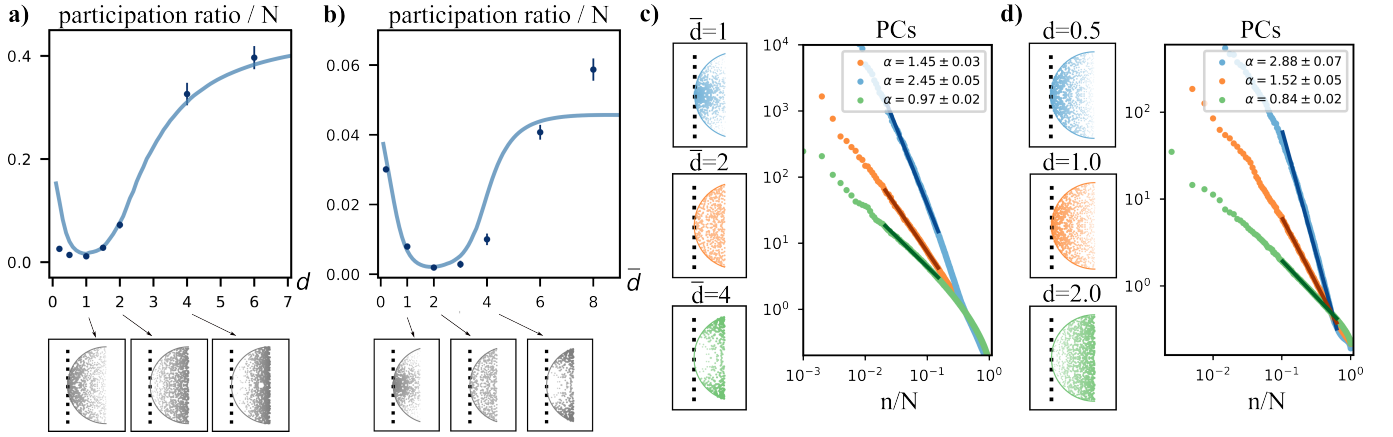


Figure 7. Strongly non-normal ensemble. (a-b) are analogous to Fig. 4(a-b), while (c-d) are analogous to Fig. 5(a) and Fig. 5(c). The same eigenvalue distributions are considered, but with strongly non-orthogonal eigenvectors. (a-b) participation ratio of the equal-time (a) and long time-window (b) covariance. $\delta = 0.01$. Markers: simulation. Solid line: theory for our original ensemble at $\nu = 0.8$ (a) and $\nu = 0.9$ (b), shown for comparison. (c-d) Principal components spectrum for the long time-window (c) and equal-time (d) covariance.

derived analytically how the shape of the eigenvalue distribution controls the network dynamics. One important property is the density of nearly-critical eigenvalues. This controls the power-law exponents characterizing the time-decay of correlation and response functions (II A) and the slope of the neuronal activity's principal components spectrum (II C). For the principal components spectrum, previous work [9] has shown that second order motifs are unable to alter its power-law decay exponent. In the density of nearly critical eigenvalues, we have identified a structural property of the connectivity that can instead control this exponent, in particular tuning it to the value observed in V1 of mice, which is argued to be optimal for encoding visual stimuli [17].

Exposing an analogy with classical critical phenomena, we have defined the system's effective spatial dimension as the exponent controlling the scaling of nearly critical eigenvalues. We have shown how this effective dimension is directly linked to the exponents characterizing the aforementioned power-laws in the network dynamics. Our work thus exposes how power-law exponents can be used as a minimal and robust measure linking observable dynamics to properties of the network's connectivity. Note that a spectral definition of effective spatial dimension has been previously proposed [40], but only in the case of symmetric networks [41, 42], whose connectivity has real eigenvalues and orthogonal eigenvectors. Our work extends this analogy to the class of asymmetric networks, which in general have complex eigenvalues and non-orthogonal eigenvectors.

We have also characterized two transition effects controlled by the shape of the eigenvalue distribution. The density of nearly critical modes controls a transition from high to low dimensional dynamics (II B). At a specific density, an optimum in dimensionality reduction is obtained. Furthermore, the maximum oscillation frequency of nearly critical modes controls a transition from power-

law to exponential time-decay in the autocorrelation and autoresponse functions (II A).

In short, through controlling the eigenmode statistics, our work allows modeling structures in a connectivity that have important consequences for the network dynamics. We have shown how this modeling approach is not in contrast, but rather complements the traditional approach, which fixes structure through the abundance of connectivity motifs. On one hand, in II B we have shown that shaping the eigenmode statistics has mainly subleading effects on the motifs statistics. On the other hand, to leading order, only correlations associated with reciprocal motifs are affected. In particular, in section III A we have shown how these are controlled by the relative spread of the eigenvalue distribution along the real and imaginary axis. This property of the eigenvalue distribution can be set to a large extent independently from the density of nearly critical eigenvalues, which is instead the property controlling the dynamical effects described in this work. Furthermore, any other second order motif can be added as a low-rank perturbation to the connectivity [9].

Finally, in III C we have extended our results to connectivities in the strongly non-normal regime. With this extension, our random matrix ensemble includes the archetypal Gaussian ensemble, but largely extends it by controlling the shape of the eigenvalue distribution and the degree of non-orthogonality of the eigenvectors. This has allowed us to analytically explore a wider range of possible network dynamics.

B. Outlooks

Connectivity motifs are typically composed of a few neurons. This property makes them amenable to mea-

sure with methods such as dual or quadrupole whole-cell recordings, which can assess with high precision the strength of connection between few neurons per time. Our work suggests that there may be additional connectivity structures, causing important dynamical consequences, which are more collective in nature and thus cannot be captured by the motifs approach. Exposing these structures requires inspecting the connectivity's spectral properties, in particular its eigenvalue distribution. We therefore advocate for spectral analysis as a fundamental, complementary tool for characterizing structure in a network's connectivity. Spectral analysis could be accessible to methods obtaining snapshots of the full microcircuit within a cortical area [43, 44]. Besides experimental data, a good testing field for methods of spectral analysis could be digital reconstructions of cortical microcircuits, which are built to have a high degree of biological realism [45].

Typical neuronal network simulations or analytical studies define connectivity by fixing some of its properties based on experimental evidence, while modeling the remaining synaptic variability as random. Typical properties being constrained are the mean strength of connections, their variance and the abundance of certain connectivity motifs. Without overwriting these constraints, we have here proposed a method to fix further structure in the connectivity by shaping its eigenmode distribution. The properties of the eigenvalue distribution could be constrained so that the network reproduces basic dynamical behaviors observed in brain networks. We have given as an example the power-law exponent observed in the decay of the neuronal activity's principal components spectrum in V1 of mice [17]. The validity of this constraint, as opposed to others potentially reproducing the same behavior, could be tested by checking whether the network reproduces other results from the same experiment. For example, the fact that the principal components' slope becomes less steep as the dimensionality of the visual inputs is increased. On another note, a simulation study has shown that an echo state network could reproduce the experimental results when driven at the edge of criticality [46]. It would be interesting to perform spectral analysis on the effective connectivity of this model, and see if this result can indeed be characterized in terms of a change in the eigenmode statistics. The effective connectivity is here intended as the one obtained by linearizing the network equations around its operational point.

Comparing to experimental data may require considering more realistic network models, for example implementing sparse connections and inhibitory and excitatory populations. The simplicity of the here studied model had the purpose of gaining analytical insights on the network dynamics. However, our methods for initializing connectivity in eigenmode space have an efficient numerical implementation that could be transferred to more complex models. For example, one could consider a connectivity of the form $S \odot (J + M)$ [47], with S

a Boolean random matrix indicating the presence of a synapse, for example implementing sparse connectivity, and M a low rank matrix encoding the inhibitory and excitatory mean synaptic strengths [9, 48]. Our original connectivity J would then represent fluctuations of the synaptic strengths. One could expect some of our results to not change qualitatively, even in this more complex setting. For example, it has been shown that low rank perturbations such as M do not alter the power-law decay in the principal components spectrum [9]. Other possible extensions of our model include non-linear dynamics and a structured input, such as, for example, the natural images utilized in the aforementioned experiment [17].

Recent works have shown that the large-scale statistics of neuronal recordings seem to approach a non-Gaussian fixed point [14, 49]. These results call for a renormalization group analysis of network models. Progress has been made in this direction by identifying an analogy between connectivity eigenmodes and the Fourier modes typical of classical critical phenomena [40], but this idea and its application has remained constrained to symmetric networks [40–42, 50]. Here we have extended this analogy to general asymmetric networks, which have complex eigenvalues and overlapping eigenvectors. In particular, we have provided mathematical tools to compute eigenvector overlaps, which is fundamental for applying the renormalization group to networks [41]. Future work may use these tools to import the renormalization group to general asymmetric networks.

Another application of our work could be in the context of optimal connectivity initialization for training artificial networks. These networks' connectivity is typically set at random according to some distribution, whose parameters are optimized so to have a beneficial starting state for training [51, 52]. By controlling the connectivity's eigenmode statistics, one could further optimize this random initialization. In this work we have given two examples: a state of optimal dimensionality reduction of the input (IIB) and a state of optimal stimulus representation (IIC).

Finally, we note that this work is, at its very core, a theory for large random asymmetric matrices with controllable eigenmode statistics. While the main motivation is to describe neuronal networks, the potential applications may extend to networks in general and beyond, to any system in which some sort of asymmetric couplings appear.

ACKNOWLEDGMENTS

This work was partially supported by the Helmholtz Association, the Initiative and Networking Fund under project number SO-092 (Advanced Computing Architectures, ACA), and the German Federal Ministry for Education and Research (BMBF Grant 01IS19077A).

Appendix A: Connectivity statistics

1. Details on the definition of the eigenmode statistics

Let us give the remaining details on the definition of the eigenmode statistics, presented in Section I. For simplicity, let us consider N even. Generalizing to N odd is straightforward. The realness of the elements of J imposes the condition that for any complex λ_α and V_α , there is an eigenmode index α^* such that $\lambda_{\alpha^*} = \lambda_\alpha^*$ and $V_{\alpha^*} = V_\alpha^*$. Note that since eigenmodes are randomly drawn in our ensemble, the probability that an eigenmode is real has null measure. Therefore we can assume all eigenmodes to be complex. By the constraint of real-valued J we only have $N/2$ eigenmodes that are independent. We assign these eigenmodes to the first $\alpha = 1, \dots, N/2$ of the eigenmode indices. The corresponding complex conjugate eigenmodes are assigned the index $\alpha^* = \alpha + N/2$. The first $N/2$ eigenvalues are drawn independently according to the desired distribution $p(\lambda)$. The remaining half is obtained by complex conjugation.

The matrix of eigenvectors V is a linear combination of O and G . The scheme by which these two matrices are defined is the same. Let us consider, for example, G . Only the first $\alpha = 1, \dots, N/2$ eigenvectors are independent, and each has a real and an imaginary component. So we need to draw $\frac{N}{2}2N = N^2$ random variables. We draw a real matrix γ whose entries $\gamma_{i\alpha} \sim \mathcal{N}(0, 1/N)$ are independent, normally distributed variables. The first $\alpha = 1, \dots, N/2$ vectors $G_{\cdot,\alpha}$ are then defined as

$$G_{\cdot,\alpha} = \frac{1}{\sqrt{2}}\gamma_{\cdot,\alpha} + \frac{i}{\sqrt{2}}\gamma_{\cdot,\alpha+N/2}$$

In words, the first $\alpha = 1, \dots, N/2$ columns of γ constitute the real part of the vectors $G_{\cdot,\alpha}$, the remaining columns $\alpha + N/2$ constitute the imaginary part. The remaining vectors G_{\cdot,α^*} are obtained through complex conjugation.

The matrix O is defined in the same way, substituting $G \rightarrow O$ and $\gamma \rightarrow o$. The only difference is that o is a real orthonormal matrix, drawn from the Haar distribution (i.e. the uniform distribution over orthogonal matrices). One can easily check that O satisfies the complex orthonormality relation $OO^\dagger = \mathbb{I}$.

Let us note that here we considered eigenvalue distributions for which the mean $\langle \lambda \rangle = 0$. A non-vanishing mean is trivial, as it amounts to sending $J \rightarrow J + \langle \lambda \rangle \mathbb{I}$, which can be reabsorbed in the definition of the leak term $-x \rightarrow -(1 - \langle \lambda \rangle)x$ in Eq. (1).

We finally comment on J being diagonalizable, and on the left eigenvectors' matrix being the inverse of the right eigenvectors' matrix (cf. Eq. (3)). The subset of non-diagonalizable matrices has null measure. Therefore it has null probability, unless one assumes some very specific distribution that is singular on the subset, which is neither the case for our ensemble nor for the archetypal Gaussian ensemble. The same reasoning applies to the

subset of matrices that have degenerate or null eigenvalues, or both. Therefore, left and right eigenvectors are inverse of each other if properly normalized. Note that here we are modeling the random part of a network's connectivity. In this case, we have shown that the aforementioned properties can be reasonably assumed. This is not necessarily the case, instead, if one is modeling specific structures that are added on top of the random connectivity, such as, for example, low rank perturbations [39].

2. Insights into the non-normality parameter ν

Here we give further intuition regarding the non-normality parameter ν and the specific definition Eq. (5) of the eigenvectors. This also allows us to get better insights into why the synaptic gain g diverges in the strongly non-normal regime $\nu \rightarrow 1$.

It is instructive to look at a naive approach in defining the eigenvector statistics. As we stated in Section I, we want to be agnostic regarding the direction taken by the random eigenvectors in neuronal space. The simplest - but too naive - way of implementing this would be to initialize $V = G$ as random Gaussians, rather than $V = O + \nu G$ as in Eq. (5). The problem is that eigenvectors defined in this way take on too random directions, having too strong overlaps. This causes the synaptic gain g to take on arbitrarily large values, when it should instead be of order unity to have physical meaning. One helpful way to visualize this is by looking at the eigenvalues of V (Fig. A1(a)). For $V = G$, these are uniformly distributed in a circle, and can get arbitrarily close to zero (Fig. A1(a), top left). This means V^{-1} , which also appears in the definition of the connectivity J , Eq. (3), can have arbitrarily large eigenvalues, and is thus unbounded, causing also g to be unbounded as a consequence. On the other hand, notice that in the trivial case of a normal network, $V = O$, the eigenvalues are exactly constrained to the unit circle, and the problem does not occur (Fig. A1(a), bottom left). To have a well defined connectivity with $g = \mathcal{O}(1)$, we introduce non-orthogonality in the eigenvectors gradually, shifting away from the orthogonal case by increasing ν , through the choice $V = O + \nu G$. Notice that in this case the eigenvalues of V cannot get arbitrarily close to zero, but are constrained to be outside of an inner circle, which will shrink back to zero as $\nu \rightarrow 1$ (Fig. A1(a), top right). We observe the same mechanism occurring in the eigenvectors of the archetypal connectivity (Fig. A1(a), bottom right). Notice that in this case the inner circle has a very small radius, which in our approach would correspond to values of ν very close to 1 and a nonphysical synaptic gain $g = \mathcal{O}(\sqrt{N})$, diverging with the system size. In fact, as discussed in III C, such strong degree of non-normality in the archetypal J is only achieved through a fine-tuned correlation between eigenvalues and eigenvectors, which ensures that all diverging contributions in

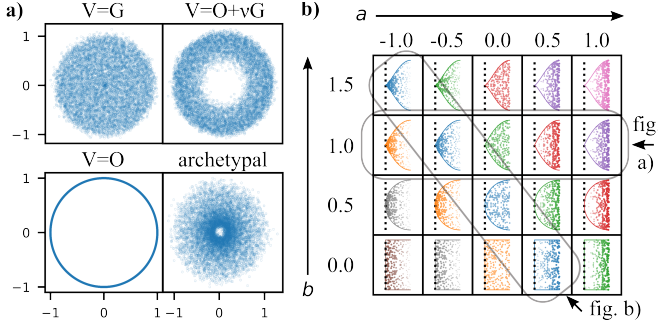


Figure A1. (a) Eigenvalues of the normalized eigenvector matrix V , for different choices of V . Parameters: $N = 10^2$. We show eigenvalues from 10^2 independent realizations of the eigenvectors. For the case $V = O + \nu G$, we use a value of $\nu = 0.8$. (b) Grid showing different distributions of nearly critical eigenvalues for varying a and b . Distributions with the same $d = a + b + 1$ share the same color (diagonals). We highlight the eigenvalue distributions used for the simulations in Fig. 3(a) (fixed b and varying a , i.e. varying d) and in Fig. 3(b) (fixed d and varying b).

Eq. (3) are tightly balanced.

3. Eigenvalue distributions used in simulations

Here we report the precise eigenvalue distributions used for the simulation of the dynamical quantities considered in Section II. Note that only the shape of the distribution near criticality is important in determining the scaling properties of dynamical quantities. Such shape has been already reported in the main text and figures. The choice of the distribution for eigenvalues further away from criticality is arbitrary and irrelevant. We report it below for completeness.

For all quantities controlled by the exponent d , that is the density of nearly critical modes along the real axis, we used the following eigenvalue distribution

$$p(\mathbf{k}) = k_x^a \theta \left(S \left(1 - (1 - k_x)^2 \right)^b - |k_y| \right) \quad \forall k_x \leq 1, \quad (\text{A1})$$

with θ being the Heaviside function. Note that A1 obeys the asymptotic scaling 10 and 12 for nearly critical eigenvalues, with $d = a + b + 1$. The parameter S allows to stretch the distribution along the imaginary axis. It is fixed to 1 in all simulations, unless stated otherwise. In Fig. A1(b) we show the distribution for the first half of the eigenvalues ($0 < k_x < 1$), as a function of the parameters a and b . The remaining half of the eigenvalues, with $1 < k_x < 2$ and thus further away from criticality, are drawn in a symmetric manner: we send $k \rightarrow 2 - k$, draw the new variable according to Eq. (A1), and transform back to the original variable (see for example the distributions shown in Fig. 2). As stated above, the precise shape of the eigenvalue distribution in this second half of the complex plane is irrelevant. Thus, the specific choice

of drawing eigenvalues in a symmetric manner is only taken for technical convenience, because then $\langle \lambda \rangle = 0$ and there is no need to rescale the leak term in Eq. (1) (see A1). In fact, even the precise shape of the distribution of the first half of the eigenvalues, Eq. (A1), is irrelevant: Only its limiting behavior for $k_x \rightarrow 0$ is important. The specific shape of the distribution has been chosen because for $a = 0$ and $b = 0.5$ it corresponds to a uniform elliptical distribution, as that of the archetypal J .

For all quantities controlled by the exponent \bar{d} , that is the density of nearly critical modes along the radial direction, we used the following eigenvalue distribution

$$p(\rho, \phi) = \rho^{\bar{d}-1} \theta \left(\arccos \left(\frac{\rho}{2} \right) - |\phi| \right) \quad \forall \rho \leq 1 \quad (\text{A2})$$

where $k \equiv \rho e^{i\phi}$. Note the expression in the Heaviside function constrains eigenvalues to lie within a circle. We fixed this shape for convenience, because for $\bar{d} = 2$ it reduces to the uniform distribution on the circle, as that of the archetypal J . Again, the exact shape of the distribution away from criticality is irrelevant, but we report it here for completeness. The remaining eigenvalues in the first half of the circle, i.e. with $1 < \rho < \sqrt{2}$, are drawn according to Eq. (A2), but are rejected and redrawn if they fall out of the semicircle, that is if $k_x > 1$. The remaining half of the eigenvalues are drawn symmetrically, as discussed in the paragraph above.

4. Strongly non-normal regime

Here we report details on the method presented in III C, to numerically implement connectivities in the strongly non-normal regime that have a desired shape of the eigenvalue distribution. The method produces the distributions presented in A3.

We start by initializing the archetypal Gaussian J , with $g = 1$ and $\tau = 0$. Its eigenvalues λ_α and associated right and left eigenvectors V_α and V_α^{-1} are derived numerically. The eigenvalues λ are uniformly distributed within a circle of unit radius. We start from this distribution and continuously shift the eigenvalues into some new position, so that they follow a new desired distribution. The continuous shift of the eigenvalues preserves to some extent the correlation structure between eigenvalues and eigenvectors, which in the strongly non-normal regime is necessary to have a synaptic gain $g = \mathcal{O}(1)$.

We first focus on producing the eigenvalue distribution Eq. (A1). This distribution is characterized by the parameters S , b and d (or equivalently a). The starting uniform circular distribution has parameters $S_0 = 1$, $b_0 = 0.5$ and $d_0 = 1.5$. Consider $k = 1 - \lambda$. To produce the eigenvalue distribution Eq. (A1) we shift the

eigenvalues $k \rightarrow \bar{k}$ through the transformation

$$\bar{k}_x = k_x^{\frac{d_0}{d}} \quad (\text{A3})$$

$$\bar{k}_y = k_y \frac{B(\bar{k}_x; S, b)}{B(k_x; S_0, b_0)} \quad (\text{A4})$$

where we defined the distribution's boundary function

$$B(k_x; S, b) \equiv S \left(1 - (1 - k_x)^2\right)^b.$$

This transformation is applied to all eigenvalues with $k_x \leq 1$. The remaining half of the eigenvalues, with $1 < k_x < 2$, are transformed in the symmetric manner described in A3. Intuitively, Eq. (A3) readjusts the eigenvalues closer or further to the critical point according to the new d . Eq. (A4) rescales the imaginary part so that it fits the new boundary of the distribution.

To obtain the distribution Eq. (A2) we use an analogous method, only that the transformation is performed on the polar coordinates of $k = \rho e^{i\phi}$. The target distribution is characterized by the parameter \bar{d} , and the original distribution has a parameter $\bar{d}_0 = 2$. We apply the transformation

$$\bar{\rho} = \rho^{\frac{\bar{d}_0}{\bar{d}}}$$

$$\bar{\phi} = \phi \frac{B(\bar{\rho})}{B(\rho)}$$

with boundary function

$$B(\rho) \equiv \arccos\left(\frac{\rho}{2}\right)$$

This transformation is applied to all eigenvalues with $\rho \leq 1$. As stated in A3, the shape of the distribution for eigenvalues further from criticality is arbitrary and irrelevant. We give it here for completeness. The remaining eigenvalues with $1 < \rho < \sqrt{2}$ which also are in the first semicircle $k_x \leq 1$ are left untouched. The remaining eigenvalues in the second semicircle are transformed in the symmetric manner described in A3.

5. Derivation of the synapctic statistics

We develop a method to compute moments (or cumulants) of the matrix elements of J . The details are reported in Section I of the Supplemental Material [31]. Here we summarize the main ideas behind the method.

Looking at the definition Eq. (3), we can see that this involves being able to compute moments of the elements of the eigenvector matrix $V = O + \nu G$ and its inverse V^{-1} (commonly called the matrices of the right and left eigenvectors, respectively). For example, computing the second moment of J corresponds to

$$\langle J_{ij} J_{hk} \rangle = \sum_{\alpha\beta} \langle \lambda_\alpha \lambda_\beta \rangle_\lambda \left\langle V_{i\alpha} V_{\alpha j}^{-1} V_{h\beta} V_{\beta k}^{-1} \right\rangle_{O,G}$$

To proceed, we note that the inverse can be written as the infinite series

$$V^{-1} = \sum_{n=0}^{\infty} (-\nu)^n (O^\dagger G)^n O^\dagger,$$

where we used that O is unitary. Computing a certain moment of V and V^{-1} thus corresponds to computing an infinite number of moments of O and G . Being Gaussian, the moments of G can be computed using Wick calculus [53], that is using the known result that moments of G factorize into the expectation of pairs of G , summing over all possible ways of pairing the G s. Similarly, moments of O can be computed using Weingarten calculus [54–56], the analogous of Wick calculus for orthogonal matrices. Weingarten calculus is more complicated, but in the limit of large N it reduces to leading order to Wick calculus [54].

There is still an infinite number of moments to compute and, at each order of ν , a large number of terms arising from the combinatorics involved in Wick calculus. At each order of ν , however, only a few terms are of leading order in N . Using a Feynman-diagram representation [53], we are able to keep track of these leading order terms, which can be identified based on the topology of the associated diagrams. Once the terms of leading order in N are computed for any given order of ν , we are able to resum all orders of ν exactly. Note that therefore our results are exact in ν and perturbative in N , which is naturally large.

With this method, we compute the second moments of J , Eq. (6) and Eq. (7). In IE of the Supplemental Material [31], we also compute the third cumulants of J . We do not compute explicitly higher order moments of J . Computing these would involve considering subleading order deviations of Weingarten calculus from Wick calculus. However, we are able to use the properties of the full Weingarten calculus to prove the results presented in IIIB, i.e. identifying which higher order moments do not vanish, and proving that these non-vanishing moments are still of subleading order in N .

Appendix B: Derivation of dynamical quantities

Here we give details on the derivation of the dynamical quantities considered in Section II.

1. Autocorrelation and autoresponse

Let us start by considering the system's linear response matrix $R(t)$, which is the Green function of Eq. (1). In frequency domain this is defined as the solution to

$$(i\omega \mathbb{I} + \mathbb{I} - J)R(\omega) = \mathbb{I}, \quad (\text{B1})$$

which is

$$R(\omega) = (i\omega \mathbb{I} + \mathbb{I} - J)^{-1}. \quad (\text{B2})$$

Using the eigenmode decomposition of J , Eq. (3), we can rewrite Eq. (B2) as

$$R_{ij}(\omega) = \sum_{\alpha} \frac{1}{i\omega + k_{\alpha}} V_{i\alpha} V_{\alpha j}^{-1} \quad (\text{B3})$$

which in time domain reads

$$R_{ij}(t) = \sum_{\alpha} \exp(-k_{\alpha} t) V_{i\alpha} V_{\alpha j}^{-1} \quad (\text{B4})$$

The expression for the population averaged autoresponse Eq. (8), considered in II A, directly follows from computing $r(t) = \frac{1}{N} \sum_i R_{ii}(t)$, noticing that $\sum_i V_{i\alpha} V_{\alpha i}^{-1} = \delta_{\alpha,\alpha} = 1$. The latter identity makes $r(t)$ independent of the eigenvectors.

Let us now consider the time-lagged covariance matrix $C_{ij}(t) \equiv \langle x_i(t) x_j(0) \rangle_{\xi}$. This can be derived by plugging into its definition the formal solution $x_i(t) = \int_{t'} \sum_j R_{ij}(t-t') \xi_j(t')$ and averaging over the noise. In frequency domain, the result is

$$C(\omega) = (i\omega \mathbb{I} + \mathbb{I} - J)^{-1} (i\omega \mathbb{I} + \mathbb{I} - J)^{-\dagger} \quad (\text{B5})$$

Using the eigenmode decomposition of J , Eq. (3), we can rewrite Eq. (B5) as

$$C_{ij}(\omega) = \sum_{\alpha\beta} F_{\alpha\beta}(\omega) V_{i\alpha} \left(\sum_h V_{\alpha h}^{-1} V_{\beta h}^{-1} \right) V_{j\beta},$$

$$F_{\alpha\beta}(\omega) \equiv \frac{1}{(\omega - ik_{\alpha})(\omega + ik_{\beta})} \quad (\text{B6})$$

which in time domain reads

$$C_{ij}(t) = \sum_{\alpha\beta} F_{\alpha\beta}(t) V_{i\alpha} \left(\sum_h V_{\alpha h}^{-1} V_{\beta h}^{-1} \right) V_{j\beta},$$

$$F_{\alpha\beta}(t) \equiv \frac{\theta(t) \exp(-k_{\alpha} t) + \theta(-t) \exp(k_{\beta} t)}{k_{\alpha} + k_{\beta}}. \quad (\text{B7})$$

The population averaged autocorrelation considered in II A is given by $A(t) = \frac{1}{N} \sum_i C_{ii}(t)$, which reads

$$A(t) = \frac{1}{N} \sum_{\alpha\beta} F_{\alpha\beta}(t) L_{\alpha\beta}, \quad (\text{B8})$$

where we defined the so-called overlap matrix

$$L_{\alpha\beta} = \sum_i V_{i\alpha} V_{i\beta} \sum_h V_{\alpha h}^{-1} V_{\beta h}^{-1} \quad (\text{B9})$$

which is a measure of how much different modes overlap in neuronal space. It is diagonal in the case $\nu = 0$ of orthonormal $V = O$. For large number of neurons N , A is self-averaging, meaning $A \sim \langle A \rangle_{O,G}$ apart from fluctuations of subleading order in N . In the expression for A , Eq. (B8), we can therefore substitute L with $\langle L \rangle_{O,G}$. The latter we can compute using the same methods summarized in A 5 (see II A of the Supplemental Material [31] for the derivation). The result is, to leading order in N ,

$$\langle L_{\alpha\beta} \rangle = \frac{1 + \nu^2}{1 - \nu^2} \delta_{\beta,\alpha^*} - \frac{2}{N} \frac{\nu^2}{1 - \nu^2}. \quad (\text{B10})$$

As commented in II A, the first term is the only one present in the limit of orthonormal eigenvectors $\nu \rightarrow 0$, while the second term reflects a non-vanishing overlap between eigenvectors for any other $\nu \neq 0$. Eq. (9) in II A is obtained by plugging Eq. (B10) into Eq. (B8) and taking the limit of the sum over eigenvalues to an integral over their probability density, with integration measure $\mathcal{D}k \equiv p(k) dk$.

2. Dimensionality

Let us recall the definition of the participation ratio for a generic covariance matrix C

$$D \equiv \frac{(\text{Tr}[C])^2}{\text{Tr}[C^2]}. \quad (\text{B11})$$

For the equal-time covariance, C corresponds to $C(t=0)$ given by Eq. (B7), while for the long time-window covariance C corresponds to $C(\omega=0)$ given by Eq. (B6).

Equal-time covariance As noted in II B, for the equal-time covariance, the numerator $(\text{Tr}[C])^2$ corresponds to $A(t=0)^2$ given in Eq. (9), whose diverging behavior near criticality is discussed in Eq. (11). Using Eq. (B7) the expression for the denominator reads

$$\text{Tr}[C^2] = \frac{1}{N^2} \sum_{\alpha\beta\gamma\delta} F_{\alpha\beta}(t=0) F_{\gamma\delta}(t=0) L_{\alpha\beta\gamma\delta}^{(2)}, \quad (\text{B12})$$

where we defined the overlap tensor

$$L_{\alpha\beta\gamma\delta}^{(2)} = \sum_i V_{i\alpha} V_{i\gamma} \sum_j V_{j\beta} V_{j\delta} \sum_h V_{\alpha h}^{-1} V_{\beta h}^{-1} \sum_k V_{\gamma k}^{-1} V_{\delta k}^{-1}. \quad (\text{B13})$$

Also $\text{Tr}[C^2]$ is self-averaging, so we can substitute $L^{(2)}$ with $\langle L^{(2)} \rangle_{O,G}$ and compute it with the same methods used for $\langle L \rangle_{O,G}$. The full result and its derivation are lengthy and are reported in II B of the Supplemental Material [31]. Here we only report the term that dominates in the diverging behavior of $\text{Tr}[C^2]$ near criticality

$$\langle L_{\alpha\beta\gamma\delta}^{(2)} \rangle_{O,G} \sim \left(\frac{1 + \nu^2}{1 - \nu^2} \right)^2 \delta_{\beta,\alpha^*} \delta_{\gamma,\alpha^*} \delta_{\delta,\alpha}$$

which plugged into Eq. (B12) gives Eq. (16) in II B.

Long time-window covariance The reasoning for the long time-window covariance is completely analogous. By comparing Eq. (B7) with Eq. (B6) we notice that one simply needs to replace $F_{\alpha\beta}(t=0) \rightarrow F_{\alpha\beta}(\omega=0)$. This leads to the results given in II B. Notice that, while $F_{\alpha\alpha^*}(t=0) = \frac{1}{\text{Re}k_{\alpha}}$, instead $F_{\alpha\alpha^*}(\omega=0) = \frac{1}{|k_{\alpha}|^2}$, so the relevant direction along which to approach criticality is the radial one, instead of the real axis.

3. Principal components spectrum

From Eq. (B7) and Eq. (B6) we immediately see that for $\nu = 0$ the eigenvalues c_α of the equal time or long time-window covariance are, respectively, $F_{\alpha\alpha^*}(t=0) = \frac{1}{\text{Re}k_\alpha}$ and $F_{\alpha\alpha^*}(\omega=0) = \frac{1}{|k_\alpha|^2}$. Indeed, for $\nu = 0$ the eigenvectors are orthonormal and so the term $\sum_h V_{\alpha h}^{-1} V_{\beta h}^{-1} = \delta_{\beta,\alpha^*}$. From this observation follow the results discussed in II C.

Appendix C: Additional figures

Here we provide some supplementary figures. Fig. C1 shows the qualitative irrelevance of details in the eigenmode statistics beyond the density of nearly critical eigenmodes in controlling the dynamical quantities studied in Section II. Fig. C2 shows a numerical validation of our analytical predictions for the motifs statistics. The numerics for the strongly non-normal regime are also reported and compared with the predictions for our ensemble.

Further supplementary figures are provided in the Supplemental Material [31].

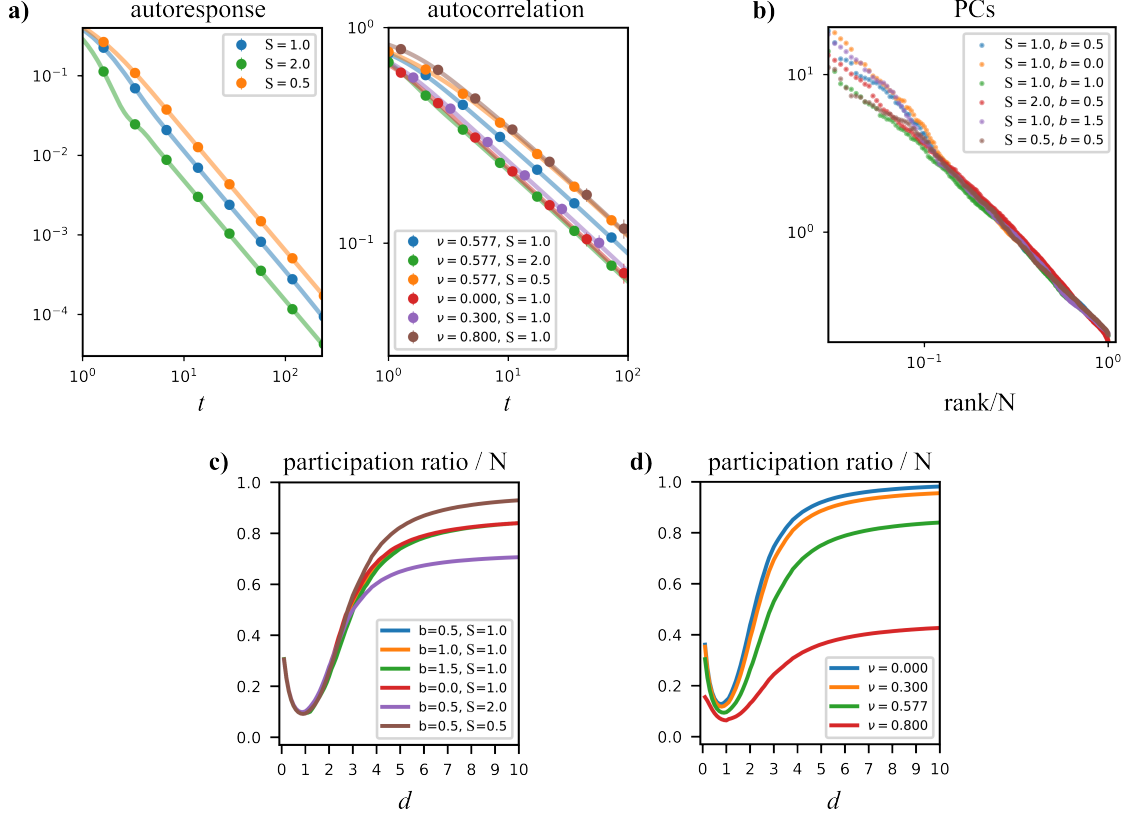
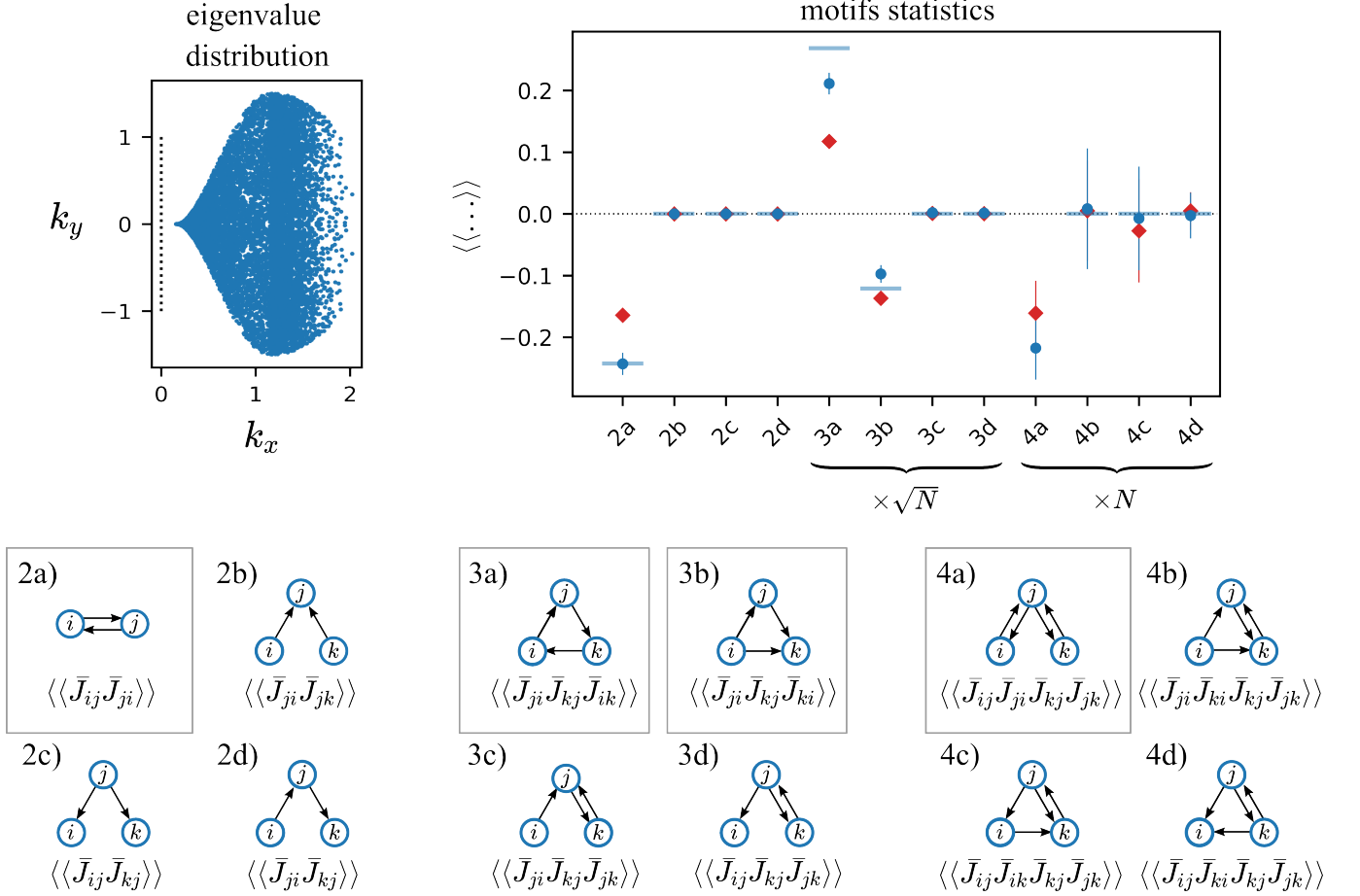


Figure C1. Irrelevance of details in the eigenvalue distribution shape and/or the degree of non-normality. (a) Autoresponse and autocorrelation, for $d = 1.5$. Shown for varying stretching factor S of the eigenvalue distribution along the imaginary axis (cfr. Eq. (A1)) and for varying degree of non-normality ν (autocorrelation only). Even if these parameters vary, the power-law decay of both functions is only controlled by d and remains the same. Markers: simulation; lines: theory. Other parameters: $b = 1.0$, $N = 10^2$. (b) Principal component spectrum of the equal-time covariance, for $d = 1.0$. Shown for varying S and varying b , controlling the boundary of the eigenvalue distribution (cfr. Eq. (12)). Even if these parameters vary, the power-law decay is only controlled by d and remains the same. Other parameters: $\nu = 1/\sqrt{3}$, $N = 4 \cdot 10^2$, $\delta = 0.01$. (c) Dimensionality of the equal-time covariance, for $\delta = 0.01$. Shown for varying S and b . Even if these parameters vary, the transition from high to low dimensionality has the same characteristic. A clear minimum is present at $d \sim 1$. In the region $d < 2$ where dimensionality $\rightarrow 0$ as $\delta \rightarrow 0$, all curves coincide. For $d > 2$, the finite limit-value taken by dimensionality can change quantitatively. Lines: theory. Other parameters: $\nu = 1/\sqrt{3}$. (d) Dimensionality of the equal-time covariance, for $\delta = 0.01$. Shown for varying ν . Though ν affects dimensionality quantitatively, the transition from high to low dimensionality has the same characteristic, with a clear minimum, present at $d \sim 1$. Lines: theory. Other parameters: $S = 1$, $b = 0.5$.



-
- [1] M. Mehta, *Random matrices*, vol. 142 of *Pure and Applied Mathematics* (Elsevier Ltd., 2004), 3rd ed.
- [2] G. Akemann, J. Baik, and P. Di Francesco, *The Oxford Handbook of Random Matrix Theory* (Oxford University Press, 2015), URL <https://doi.org/10.1093/oxfordhb/9780198744191.001.0001>.
- [3] E. P. Wigner, *Ann. Math.* **62**, 548 (1955).
- [4] H. Sompolinsky, A. Crisanti, and H. J. Sommers, *Phys. Rev. Lett.* **61**, 259 (1988).
- [5] C. van Vreeswijk and H. Sompolinsky, *Science* **274**, 1724 (1996).
- [6] D. J. Amit and N. Brunel, *Cereb. Cortex* **7**, 237 (1997).
- [7] N. Brunel, *J. Comput. Neurosci.* **8**, 183 (2000).
- [8] Y. Hu, J. Trousdale, K. Josić, and E. Shea-Brown, *J. Stat. Mech. Theory Exp.* **2013**, P03012 (2013).
- [9] Y. Hu and H. Sompolinsky, *PLOS Computational Biology* **18**, 1 (2022).
- [10] S. Song, P. Sjöström, M. Reigl, S. Nelson, and D. Chklovskii, *PLOS Biol.* **3**, e68 (2005).
- [11] J. M. Beggs and D. Plenz, *J. Neurosci.* **23**, 11167 (2003).
- [12] C. Haldeman and J. M. Beggs, *Phys. Rev. Lett.* **94**, 058101 (2005).
- [13] A. J. Fontenele, N. A. P. de Vasconcelos, T. Feliciano, L. A. A. Aguiar, C. Soares-Cunha, B. Coimbra, L. Dalla Porta, S. Ribeiro, A. J. Rodrigues, N. Sousa, et al., *Phys. Rev. Lett.* **122**, 208101 (2019).
- [14] L. Meshulam, J. L. Gauthier, C. D. Brody, D. W. Tank, and W. Bialek, *Phys. Rev. Lett.* **123**, 178103 (2019).
- [15] P. T. Sadtler, K. M. Quick, M. D. Golub, S. M. Chase, S. I. Ryu, E. C. Tyler-Kabara, B. M. Yu, and A. P. Batista, *Nature* **512**, 423 (2014), ISSN 1476-4687, number: 7515 Publisher: Nature Publishing Group.
- [16] J. A. Gallego, M. G. Perich, S. N. Naufel, C. Ethier, S. A. Solla, and L. E. Miller, *Nat. Commun.* **9**, 1 (2018).
- [17] C. Stringer, M. Pachitariu, N. Steinmetz, M. Carandini, and K. D. Harris, *Nature* **571**, 361 (2019).
- [18] B. Lindner, B. Doiron, and A. Longtin, *Phys. Rev. E* **72**, 061919 (2005).
- [19] V. Pernice, B. Staude, S. Cardanobile, and S. Rotter, *PLOS Comput. Biol.* **7**, e1002059 (2011).
- [20] V. Pernice, B. Staude, S. Cardanobile, and S. Rotter, *Phys. Rev. E* **85**, 031916 (2012).
- [21] D. Grytskyy, T. Tetzlaff, M. Diesmann, and M. Helias, *Front. Comput. Neurosci.* **7**, 131 (2013).
- [22] J. Trousdale, Y. Hu, E. Shea-Brown, and K. Josić, *PLOS Comput. Biol.* **8**, e1002408 (2012).
- [23] D. Dahmen, S. Grün, M. Diesmann, and M. Helias, *Proc. Natl. Acad. Sci. USA* **116**, 13051 (2019).
- [24] D. Dahmen, S. Recanatesi, X. Jia, G. K. Ocker, L. Campanola, T. Jarsky, S. Seeman, M. Helias, and E. Shea-Brown, *BioRxiv* (2022).
- [25] H. Sommers, A. Crisanti, H. Sompolinsky, and Y. Stein, *Phys. Rev. Lett.* **60**, 1895 (1988).
- [26] J. Aljadeff, M. Stern, and T. Sharpee, *Phys. Rev. Lett.* **114**, 088101 (2015).
- [27] J. Schuecker, S. Goedeke, and M. Helias, *Phys. Rev. X* **8**, 041029 (2018).
- [28] D. R. Chialvo, *Nat. Phys.* **6**, 744 (2010), ISSN 1745-2481, number: 10 Publisher: Nature Publishing Group.
- [29] C. G. Langton, *Physica D* **42**, 12 (1990).
- [30] N. Bertschinger and T. Natschlager, *Neural Comput.* **16**, 1413 (2004).
- [31] See Supplemental Material for supplementary figures and further details on the analytical derivations.
- [32] K. G. Wilson, *Rev. Mod. Phys.* **47**, 773 (1975).
- [33] P. C. Hohenberg and B. I. Halperin, *Rev. Mod. Phys.* **49**, 435 (1977).
- [34] U. C. Täuber, *Critical dynamics: a field theory approach to equilibrium and non-equilibrium scaling behavior* (Cambridge University Press, 2014), ISBN 9780521842235.
- [35] J. D. Semedo, A. Zandvakili, C. K. Machens, M. Y. Byron, and A. Kohn, *Neuron* **102**, 249 (2019).
- [36] S. Recanatesi, G. K. Ocker, M. A. Buice, and E. Shea-Brown, *PLOS Comput. Biol.* **15**, 1 (2019).
- [37] G. Hennequin, T. Vogels, and W. Gerstner, *Neuron* **82**, 1394 (2014).
- [38] D. Dahmen, H. Bos, and M. Helias, *Phys. Rev. X* **6**, 031024 (2016).
- [39] F. Mastrogiuseppe and S. Ostojic, *Neuron* **99**, 609 (2018).
- [40] S. Bradde, F. Caccioli, L. Dall'Asta, and G. Bianconi, *Phys. Rev. Lett.* **104**, 218701 (2010).
- [41] A. i. e. i. f. Tuncer and A. m. c. Erzan, *Phys. Rev. E* **92**, 022106 (2015).
- [42] B. A. Brinkman, *arXiv preprint arXiv:2301.09600* (2023).
- [43] M. Berning, K. M. Boergens, and M. Helmstaedter, *Neuron* **87**, 1193 (2015).
- [44] W. Yin, D. Brittain, J. Borseth, M. E. Scott, D. Williams, J. Perkins, C. S. Own, M. Murfitt, R. M. Torres, D. Kapner, et al., *Nature communications* **11**, 4949 (2020).
- [45] H. Markram, E. Muller, S. Ramaswamy, M. W. Reimann, M. Abdellah, C. A. Sanchez, A. Ailamaki, L. Alonso-Nanclares, N. Antille, S. Arsever, et al., *Cell* **163**, 456 (2015).
- [46] G. B. Morales and M. A. Muñoz, *Biology* **10** (2021), ISSN 2079-7737.
- [47] I. D. Harris, H. Meffin, A. N. Burkitt, and A. D. Peterson, *arXiv preprint arXiv:2212.01549* (2022).
- [48] J. Kadmon and H. Sompolinsky, *ArXiv* p. 1508.06486 (2015).
- [49] S. Bradde and W. Bialek, *J. Stat. Phys.* **167**, 462 (2017), ISSN 1572-9613.
- [50] L. Tiberi, J. Stapmanns, T. Kühn, T. Luu, D. Dahmen, and M. Helias, *Phys. Rev. Lett.* **128** (2022).
- [51] B. Poole, S. Lahiri, M. Raghu, J. Sohl-Dickstein, and S. Ganguli, in *Advances in Neural Information Processing Systems 29* (2016), URL <https://proceedings.neurips.cc/paper/2016/file/148510031349642de5ca0c544f31b2ef-Paper.pdf>.
- [52] J. Pennington, S. S. Schoenholz, and S. Ganguli, *ArXiv* (2017), 1711.04735.
- [53] M. Helias and D. Dahmen, *Statistical Field Theory for Neural Networks* (Springer International Publishing, 2020).
- [54] D. Weingarten, *Journal of Mathematical Physics* **19**, 999 (1978), ISSN 0022-2488, publisher: American Institute of Physics.
- [55] B. Collins and P. Śniady, *Communications in Mathematical Physics* **264**, 773 (2006), ISSN 1432-0916.
- [56] S. Matsumoto, *The Ramanujan Journal* **26**, 69 (2011),

ISSN 1572-9303.